The Astrophysical Journal, 876:27 (16pp), 2019 May 1 https://doi.org/10.3847/1538-4357/ab13ab

Time Evolution of Broadband Nonthermal Emission from Supernova Remnants in Different Circumstellar Environments

Haruo Yasuda and Shiu-Hang Lee
Department of Astronomy, Kyoto University, Kitashirakawa, Oiwake-cho, Sakyo-ku, Kyoto 606-8502, Japan; yasuda@kusastro.kyoto-u.ac.jp
Received 2019 February 7; revised 2019 March 8; accepted 2019 March 25; published 2019 April 30

Abstract

Supernova remnants (SNRs) are thought to be one of the major acceleration sites of galactic cosmic rays and an important class of objects for high-energy astrophysics. SNRs produce multiwavelength, nonthermal emission via accelerated particles at collisionless shocks generated by the interactions between the SN ejecta and the circumstellar medium (CSM). Although it is expected that the rich diversities observed in supernovae (SNe) and their CSM can result in distinct very high energy (VHE) electromagnetic signals in the SNR phase, there are only a handful of SNRs observed in both GeV and TeV γ-rays so far. A systematic understanding of particle acceleration at SNRs in different ambient environments is therefore limited. Here we explore nonthermal emission from SNRs in various circumstellar environments up to 5000 yr from explosion using hydrodynamical simulations coupled with efficient particle acceleration. We find that time evolution of emission characteristics in the VHE regime is mainly dictated by two factors: the number density of the target particles and the amplified magnetic field in the shocked medium. We also predict that the Cherenkov Telescope Array (CTA) will have sufficient sensitivity to detect VHE γ-rays from most young SNRs at distances $\lesssim$5.0 kpc. Future SNR observations with CTA will thus be promising for probing the CSM environment of SNe and hence their progenitor properties, including the mass-loss history of massive stars.

Key words: acceleration of particles – cosmic rays – ISM: supernova remnants – radiation mechanisms: nonthermal

1. Introduction

Since Baade & Zwicky (1934) suggested the relation between supernovae (SNe) and cosmic rays (CRs), supernova remnants (SNRs) have been studied as the accelerators of Galactic CRs below the "knee" energy ($\sim$3 PeV). One of the most successful theories currently for the particle acceleration mechanism is the so-called diffusive shock acceleration (DSA; e.g., Fermi 1949; Drury 1983; Caprioli et al. 2010a, 2010b), which has been widely studied in the past couple of decades; nevertheless, there still remains much to be understood in the details of the microphysical processes.

SNRs are commonly detected in multiwavelength observstions, and some have been found to shine in a broad range of frequencies from radio all the way to TeV γ-rays. In general, they emit broadband nonthermal electromagnetic radiation owing to their interactions with the interstellar matter (ISM) or circumstellar medium (CSM). The radio and nonthermal X-rays are believed to be produced by relativistic electrons through synchrotron radiation. The γ-rays can originate both from relativistic electrons through inverse Compton scattering (IC) and bremsstrahlung and from relativistic protons through the π^0-decay channel from proton–proton inelastic scatterings, which are usually regarded as the *leptonic* and *hadronic* processes, respectively.

Figure 1 shows the spectral energy distribution (SED) of SNRs that have been observed so far in the GeV-to-TeV energy range and the references are summarized in Table 1. The top panel shows the overall SED from radio to 1 PeV, and the bottom panel shows the γ-ray SED from 10 MeV to 1 PeV. In most cases, the radio and nonthermal X-ray spectrum can be satisfactorily reproduced by a synchrotron origin regardless of SNR age, but the differences in the observed γ-ray spectra among these SNRs are remarkable. Whether the γ-rays are produced by either a *hadronic* or *leptonic* (or both) channel has a large implication on the particle acceleration mechanism, such as the injection efficiencies of the suprathermal particles, the maximum energy of the accelerated particles, and the overall acceleration efficiency. These aspects can vary significantly among different individual SNRs depending on their ambient environment, age, and progenitor system, which need to be fully understood in a consistent picture in order to examine the SNR population as a dominant source of Galactic CRs. However, the model interpretation is still often found to be controversial and remains a subject for discussion.

A general picture has been proposed by recent works (e.g., Yuan et al. 2012) that the observed properties of the γ-ray emission from SNRs are mainly determined by the gas density in their surrounding environments, i.e., the dominant component of the γ-ray flux is IC if the SN occurred in a relatively tenuous medium, while the π^0-decay component dominates in a denser medium such as a molecular cloud. These results, however, are usually based on phenomenological fitting of the observed photon SED from individual SNRs using simple one-zone models. From the theoretical point of view, previous works (e.g., Fang & Zhang 2008; Tang et al. 2016; Gaggero et al. 2018) also follow the long-term time evolution of broadband emission, but assumptions and simplifications like the one-zone hydrodynamical model and simple power-law CR spectrum are usually employed in these calculations. Currently, there are few studies that follow the long-term time evolution of the broadband emission together with the hydrodynamical evolution of the SNRs coupled to a self-consistent treatment of DSA at the shocks. Here, using a multizone hydrodynamical simulation coupled with an efficient particle acceleration, we generate a grid of evolutionary models of SNRs interacting with various kinds of ISM/CSM environments up to a few times 10^3 yr over an observation-based parameter space. Our

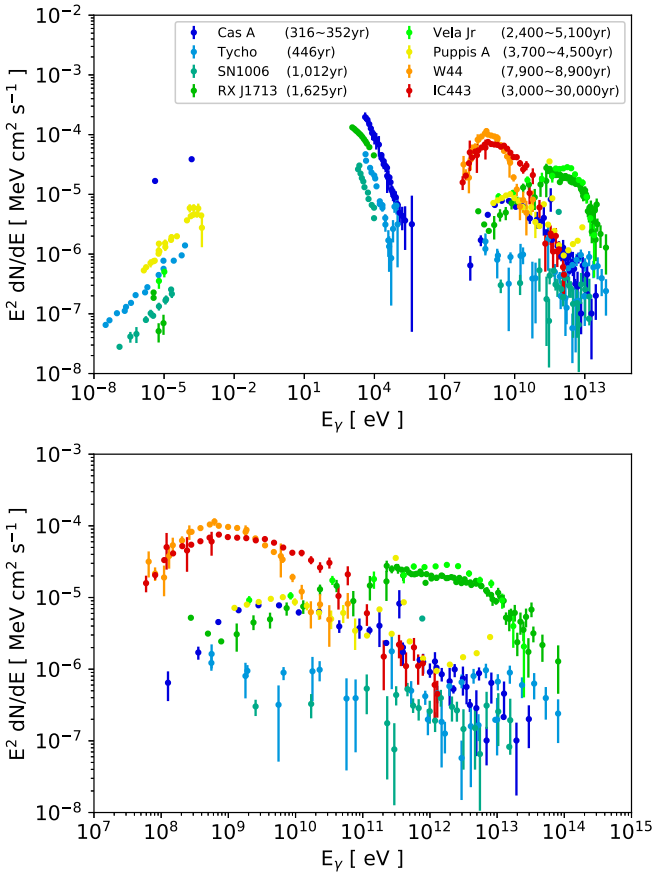

Figure 1. Top panel: multiwavelength SED of the SNRs whose γ-ray flux is detected. The color of data points almost represents the SNR age; the redder the color becomes, the older the age of SNRs becomes. Bottom panel: same as the top panel, but the energy range is from 10 MeV to 1 PeV.

results are analyzed to explore general trends in the characteristics of the time-evolving SED that can be used in the future as a probe of the structure of the surrounding environment. Based on our results, we also predict the observability of typical young core-collapse (CC) and Type Ia SNRs by the upcoming ground-based VHE γ-ray observatory the Cherenkov Telescope Array (CTA).

In Section 2, we introduce our numerical method for the evolutionary model of SNRs and the range of models adopted for the ambient environment. Section 3 describes our results and interpretations from the calculation, including the time evolution of the SNR dynamics and the multiwavelength spectra, and provides a comparison to the currently available observational data. Concluding remarks and a summary can be found in Section 4.

2. Method

2.1. Simulation Code and Included Physics

We develop a hydrodynamical code to investigate the effect of CSM interaction on the long-term evolution of nonthermal radiation from SNRs. The code performs 1D spherically symmetric hydro simulations on a Lagrangian mesh based on the VH-1 code (e.g., Blondin & Ellison 2001) coupled with a semianalytic nonlinear DSA (NLDSA) calculation (see, e.g., Blasi 2004; Caprioli et al. 2010a, 2010b) similar to the framework first introduced in the *CR-hydro-NEI* code (see, e.g., Lee et al. 2012). The time evolution of the SNR is numerically calculated through a Lagrangian hydrodynamics simulation starting from a self-similar model for the SN ejecta as the initial condition. The expansion of the SNR into whatever ambient environment adopted in a model is then followed by the hydro simulation, from which the shock dynamics is traced in real time as an input for an NLDSA calculation. The NLDSA part provides a solution for the accelerated CR, which feedbacks to the hydrodynamics through an effective gamma approach, i.e., a modified equation of state in the shocked medium (Blondin & Ellison 2001), as well as the occurrence of a shock precursor.

NLDSA is sensitive to the shock velocity and the gas density and the magnetic field strength in the upstream environment, so we improve their code to calculate the DSA process and its hydrodynamical feedbacks at the shock every time the shock sweeps up gas in a new (unshocked) grid. This is particularly important in the case of a structured ambient medium such as a confined CSM due to an episodic mass loss from a massive star (see Section 3.4).

In the NLDSA calculation, we obtain the phase-space distribution function $f(x, p)$ of the accelerated protons by solving the following diffusion-convection equation written in the shock rest frame (e.g., Caprioli et al. 2010a, 2010b; Lee et al. 2012), assuming a steady-state[1] distribution isotropic in momentum space,

$$[u(x) - v_A(x)]\frac{\partial f(x,p)}{\partial x} - Q(x,p) = \frac{\partial}{\partial x}\left[D(x,p)\frac{\partial f(x,p)}{\partial x}\right] + \frac{p}{3}\frac{d[u(x)-v_A(x)]}{dx}\frac{\partial f(x,p)}{\partial p}, \quad (1)$$

where $D(x, p)$, $u(x)$, $v_A(x)$ are the spatial diffusion coefficient, gas velocity, and Alfvén speed in the shock rest frame at each position x. Hereafter, we label each quantity with a subscript "0," "1," and "2" denoting values far upstream ($x = -\infty$), immediately upstream ($x = 0^-$), and immediately downstream ($x = 0^+$) from the shock, respectively. We assume a Bohm diffusion for the accelerating particles in this work, such that $D(x, p) = pc^2/3eB(x)$, where $B(x)$ is the local magnetic field strength at position x. The magnetic field is self-consistently calculated with magnetic field amplification (MFA) due to self-generated turbulence through resonant CR streaming instability (e.g., Bell 1978; Caprioli et al. 2009b). Following Blasi (2004) and Blasi et al. (2005), we adopt the "thermal-leakage" injection model for the DSA injection rate $Q(x, p)$ such that

$$Q(x,p) = \eta\frac{n_1 u_1}{4\pi p_{\rm inj}^2}\delta(x)\delta(p - p_{\rm inj}), \quad (2)$$

where $\eta = \{4/(3\sqrt{\pi})\}(S_{\rm sub} - 1)\chi_{\rm inj}^3 e^{-\chi_{\rm inj}^2}$ and $S_{\rm sub} = (u_1 - v_{A,1})/(u_2 + v_{A,2})$ is the effective compression ratio that the streaming particles experience at the subshock position ($x = 0$). $p_{\rm inj} \equiv \chi_{\rm inj}\sqrt{2m_{\rm p}k_{\rm b}T_{\rm p}}$ is the DSA injection momentum, where $m_{\rm p} = 1.6 \times 10^{-24}$ g is the mass of the proton, $T_{\rm p}$ is the proton temperature, and $\chi_{\rm inj}$ is a free parameter constrained by

[1] We consider that it is reasonable to use the steady-state approximation as long as the dynamical timescale of the SNR is longer than the DSA acceleration timescale $t_{\rm acc}$. Known young SNRs are found to accelerate protons up to a maximum momentum $\sim$100 TeV/c or below, so that $t_{\rm acc} \sim D/u^2 \sim 1(p/100\ {\rm TeV}/c)(B/100\ \mu{\rm G})^{-1}(u/3000\ {\rm km\ s^{-1}})^{-2}$ yr, where D, u, p, B are the diffusion coefficient, the shock velocity, the particle momentum, and the amplified magnetic field, respectively. We find that the above condition can be satisfied within the scope of our models.

observations. By solving Equation (1), the distribution function at the shock position with a cutoff at a maximum momentum $p_{\rm max}$ can be written in implicit form as

$$f_1(p) = f(x=0,p) = \frac{3S_{\rm tot}}{S_{\rm tot}U(p)-1} \times \left[\frac{\eta n_0}{4\pi p_{\rm inj}^3}\exp\left(-\int_{p_{\rm inj}}^{p}\frac{dp'}{p'}\frac{3S_{\rm tot}U(p')}{S_{\rm tot}U(p')-1}\right)\right] \times \exp\left\{-\left(\frac{p}{p_{\rm max}}\right)^{\alpha}\right\}, \quad (3)$$

where $S_{\rm tot} = (u_0 - v_{A,0})/(u_2 + v_{A,2})$ is the effective total compression ratio of the CR-modified shock. The explicit expressions of $u(x)$, $v_A(x)$, $U(p)$ can be found in Lee et al. (2012) and references therein. The parameter α describes the rollover shape near the high-energy cutoff, which serves as a parameterization of the poorly understood escape process of the accelerated particles.

As for the electrons whose gyroradii are much smaller at thermal energies, the injection mechanism and efficiency relative to their proton and ion counterparts at strong collisionless shocks are still not fully understood, although a few first-principle kinetic simulations have shed new light onto this topic recently (see, e.g., Matsumoto et al. 2017, and references therein). In this work, we constrain the electron-to-proton number ratio ($K_{\rm ep}$) at relativistic momenta below the cutoff by currently available data from multiwavelength observations. Current observations of young γ-ray-emitting SNRs have constrained $K_{\rm ep}$ to a range of a few $\times 10^{-4}$ to $\sim 10^{-2}$ (e.g., H.E.S.S. Collaboration et al. 2018a). In this work, we adopt a $K_{\rm ep}$ by performing calibrations against data from prototypical Type Ia and CC SNRs (see Section 3.1).

The maximum momentum of the accelerated protons is constrained by a number of physical conditions as described below, and its value is taken to be the minimum of the momenta obtained by applying these conditions, i.e., $p_{\rm max,p} = \min\{p_{\rm max,age}, p_{\rm max,feb}\}$, which changes with time as the shock propagates and evolves. The condition for $p_{\rm max,age}$ (*age-limited*) comes from the comparison of the SNR age $t_{\rm age}$ with the DSA acceleration timescale $t_{\rm acc}$. An approximate expression for $t_{\rm acc}$ can be written as

$$t_{\rm acc} \approx \frac{3}{u_0 - u_2}\int_{p_{\rm inj}}^{p_{\rm max}}\frac{dp}{p}\left(\frac{D_0(p)}{u_0} + \frac{D_2(p)}{u_2}\right), \quad (4)$$

where $D_0(p)$ ($D_2(p)$) is the diffusion coefficient far upstream (immediately downstream) from the shock.

The condition for $p_{\rm max,feb}$ (*escape-limited*) comes from the spatial confinement of the accelerating particles, i.e., a comparison of the particle diffusion length $L_{\rm diff}$ with a free escape boundary (FEB) set at a distance $L_{\rm feb}$ upstream from the subshock. Here $L_{\rm feb} = f_{\rm feb}R_{\rm sk}$, where $f_{\rm feb}$ is typically taken between 0.1 and 0.2, motivated by currently available models of SNR observations (e.g., Caprioli et al. 2009a; Lee et al. 2012). We fix $f_{\rm feb}$ at 0.1 in this study.[2] $L_{\rm diff}$ can be obtained by the following expression:

$$L_{\rm diff} = \left\langle\frac{D(x,p_{\rm max})}{u(x)}\right\rangle = \int_{-L_{\rm feb}}^{0}\frac{dx}{L_{\rm feb}}\frac{D_0(x,p_{\rm max})}{u(x)}. \quad (5)$$

For electrons, $p_{\rm max,e}$ is further restricted by the efficient energy loss due to radiation (*loss-limited*), that is, $p_{\rm max,e} = \min\{p_{\rm max,age}, p_{\rm max,feb}, p_{\rm max,loss}\}$. The condition for $p_{\rm max,loss}$ (*loss-limited*) derives from the comparison of the acceleration timescale $t_{\rm acc}$ with the timescale of energy losses from nonthermal emission $t_{\rm loss}$. Typically, synchrotron radiation and IC dominate the energy loss of relativistic electrons; hence, we can obtain $t_{\rm loss}$ as follows:

$$t_{\rm loss} = \frac{3m_{\rm e}c^2}{4c\sigma_{\rm T}U_{\rm B,2}\gamma}\left(1 + \sum_{i=1}^{N_{\rm p}}\frac{W_i\gamma_{k,i}^2}{U_{\rm B,2}(\gamma^2+\gamma_{k,i}^2)}\right)^{-1}, \quad (6)$$

where $U_{\rm B,2} = {B_2}^2/8\pi$ is magnetic field energy density downstream and $\sigma_{\rm T}$, γ are the Thompson cross section and electron Lorentz factor, respectively. $N_{\rm p}$ is the number of components of external photon fields, and $\gamma_{k,i} = 0.53m_{\rm e}c^2/k_{\rm b}T_i$ is the critical Lorentz factor. W_i, T_i are the energy density and effective temperature of the ith component of the seed photon fields, respectively. In this study, we only consider the cosmic microwave background (CMB) radiation as the target photons for simplicity, so $W_i = 0.26\,{\rm eV\,cm^{-3}}$ and $T_i = 2.7$ K.

After the particles are accelerated at the shock, they advect with the gas flow in the downstream region assuming an effective trapping by the strong, amplified magnetic turbulence. During the advection, they lose energy in the meantime through nonthermal emission owing to interactions with the shocked ISM/CSM and the adiabatic expansion of the SNR. Following Sturner et al. (1997), the radiation loss mechanisms include synchrotron radiation, bremsstrahlung, IC for electrons, and an addition of pion productions for protons. Coulomb loss is not included in this work but can be important for sub-GeV γ-ray emission.

Using the calculated proton and electron spectra in each position at any given age, we can then calculate the broadband nonthermal emission spectra. Our code includes synchrotron, IC, thermal, and nonthermal bremsstrahlung and π^0-decay emission by the accelerated particles, taking also into account the additional contributions from secondary electrons and positrons on the synchrotron, IC, and nonthermal bremsstrahlung components. We apply Equations (D1)–(D7) in Aharonian et al. (2010) to calculate the volume emissivities for synchrotron radiation, Equations (29)–(33) in Sturner et al. (1997) for IC, Equations (26)–(28) in Sturner et al. (1997) for nonthermal electron–proton bremsstrahlung, Equations (A1)–(A7) in Baring et al. (1999) for nonthermal electron–electron bremsstrahlung, and the parameterized model presented in Kamae et al. (2006) for the π^0-decay γ-ray emission. The code also computes the thermal bremsstrahlung emission using Equation (5.14) in Rybicki & Lightman (1986). For this component, we assumed that the shocked gases are fully ionized after shock heating, so that the electron number density is $n_{\rm e}(x) = (1+f_{\rm He})\times\rho(x)/\mu{\rm m_p}$, where $\mu = 1.4$ is the mean molecular weight assuming that the number fraction of helium $f_{\rm He}$ is 10% of hydrogen in the ambient medium.

The shock-heated proton and electron temperatures are assumed to be proportional to the mass number for a collisionless shock, and they are further evolved in the

[2] In our models, $p_{\rm max}$ is typically constrained by *age-limited* for a $t_{\rm age} \leqslant 100$ yr and then becomes *escape-limited* afterward. The exact timing of the transition depends on the ambient medium into which the SN ejecta expands in the early phase (see Figures 5 and 7).

downstream region owing to adiabatic cooling/heating and equilibration through Coulomb collisions (i.e., Equations (5)–(31) in Spitzer 1965). We also include free–free absorption and synchrotron-self absorption with Equations (5.18) and (6.50) in Rybicki & Lightman (1986), which are important in the radio band. The treatment of secondary electron/positron production through $\pi^{\pm}$ decay and subsequent photon emission follows the method described in Lee et al. (2015).

After the SNR has entered the radiative phase, the shock slows down to an extent that DSA is expected to be inefficient relative to the younger stages (see, however, Lee et al. 2015 and references therein for a discussion on GeV-bright middle-aged SNRs). We do not treat the physics involved in radiative shocks in this work, and the simulations are terminated before the SNR becomes radiative. For all cases, we run the models up to an age of 5000 yr, which is still within the Sedov–Taylor phase. We also do not consider the acceleration of heavy ions and possible DSA at the reverse shock (RS) in this study. These aspects will be discussed in future works.

2.2. Models for the Surrounding Environment

In this study, we look at two classes of simple but representative models for the ambient medium around an SNR. In model A and its variants, we consider a uniform ISM-like environment, which is usually expected for a Type Ia SNR (with exceptions),

$$\rho(r) = \mu m_{\rm p} n_{\rm ISM}, \tag{7}$$

$$B(r) = B_0, \tag{8}$$

where $n_{\rm ISM}, B_0$ are the ISM proton number density and magnetic field, respectively. We use an exponential profile for the SN ejecta in these models (Dwarkadas & Chevalier 1998).

Model B and its variants adopt a power-law spatial distribution for the density in the ambient gas, which mimics the CSM created by a nonepisodic isotropic stellar wind from a massive star prior to core-collapse supernova (CCSN; Ellison et al. 2012, and references therein),

$$\rho(r) = \frac{\dot{M}}{4\pi V_{\rm w}} r^{-2}, \tag{9}$$

$$B(r) = \frac{(\sigma_{\rm w} V_{\rm w} \dot{M})^{1/2}}{r}, \tag{10}$$

where $\dot{M}$, $V_{\rm w}$, $\sigma_{\rm w}$ are the mass-loss rate, wind velocity, and ratio between the magnetic field energy density and the wind kinetic energy density, i.e., $\sigma_{\rm w} \equiv P_{\rm B}/E_{\rm kin,w} = (B^2/8\pi)/(\rho V_{\rm w}^2/2)$. We use a flat core with power-law envelope profile for the ejecta in these CCSN-like models (Truelove & McKee 1999). In both classes of models, we assume that the gas velocity and temperature of the unshocked material are constant in space.

In model C, we investigate the case of a nonsteady mass-loss history from a massive star in which a dense shell (or confined CSM) surrounding the ejecta is created owing to mass ejection from the stellar envelope during the course of a few hundred years before the CC onset. The CSM is represented by a simple combination of two wind profiles where the one in the inner region has a higher density, as follows:

$$\begin{aligned}\rho(r) &= \frac{\dot{M}}{4\pi V_{\rm w}} r^{-2} \quad (R_{\rm tr} < r) \\ &= \frac{\dot{M}_2}{4\pi V_{\rm w,2} R_{\rm tr}^2} \left(\frac{r}{R_{\rm tr}}\right)^{-n_{\rm pl,2}} \quad (r \leqslant R_{\rm tr}),\end{aligned} \tag{11}$$

where $\dot{M}_2$, $V_{\rm w,2}$, $n_{\rm pl,2}$ are the mass-loss rate, velocity, and power-law index of the wind profile from an enhanced mass loss, respectively, and $R_{\rm tr}$ is the transition radius between the normal wind and the confined CSM region. As typical values, we consider an episode in which an enhanced mass-loss ejection with $V_{w,2} \sim 1000\,{\rm km\,s^{-1}}$ occurred during the last $\sim$1000 yr before explosion, and $R_{\rm tr} \sim 1.0$ pc.

3. Results and Discussion

3.1. Calibration Models

To cross-check the robustness of the code and its capability of reproducing observations, we first consider two models, A0 and B0, with parameters chosen to match the multiwavelength observation data of the Type Ia SNR Tycho and the CC SNR RX J1713.7–3946 (hereafter RX J1713) based on the multi-wavelength emission model from previous hydro simulations presented in Slane et al. (2014) and Lee et al. (2012), respectively. Models A and B and their variants will then be generated based on these observationally calibrated models by varying the ambient environment.

Tycho is identified to be the remnant produced by the historical SN SN 1572, which is classified as a Type Ia SN from its light-echo spectrum, chemical abundance pattern inferred from the X-ray spectrum, and so on. Although it has been suggested that the ambient density around Tycho has an azimuthal gradient (Williams et al. 2013), we here assume a uniform ambient medium for simplicity. Figure 2 shows the hydrodynamical and spectral results from our best-fit calibration model. The top panel of Figure 2 shows the radial profile of the total mass density of the plasma (i.e., shocked/unshocked ISM and ejecta) at the current SNR age, $t_{\rm age} = 446$ yr. The solid line is the result from model A0, and the thin dashed line is the result when particle acceleration is not included but otherwise identical to model A0. The red, blue, and green bands are the radii of the forward shock (FS), RS, and contact discontinuity (CD) inferred from observation (Warren et al. 2005). We can see that our simulation can reproduce the FS and RS positions,[3] but not the case for the CD. If particle acceleration is efficient (i.e., small $\gamma_{\rm eff}$), however, it has been reported that Rayleigh–Taylor (R-T) instability can develop between the FS and CD (e.g., Blondin & Ellison 2001; Warren & Blondin 2013) and the CD position can possibly extend outward significantly (also see discussions in Slane et al. 2014). Our calculation can hence be considered to be in good agreement with observations on dynamics. The calculated SED at the same age is plotted in the bottom panel. The observed fluxes are overlaid in the same plot. The agreement is found to be reasonable and reproduces the result of Slane et al. (2014) in their model A. It can be seen that Tycho has a soft GeV-to-TeV

[3] As mentioned in Section 2, we only consider DSA at the FS in this work, as smoking-gun evidence of efficient DSA at the RS in SNRs is still absent. We can see in the top panel of Figure 2 the difference between the solid line and the dashed line, which show the results with and without feedback from an efficient DSA at the FS, respectively. DSA at the RS can be included in the code relatively easily when such evidence will surface in the future.

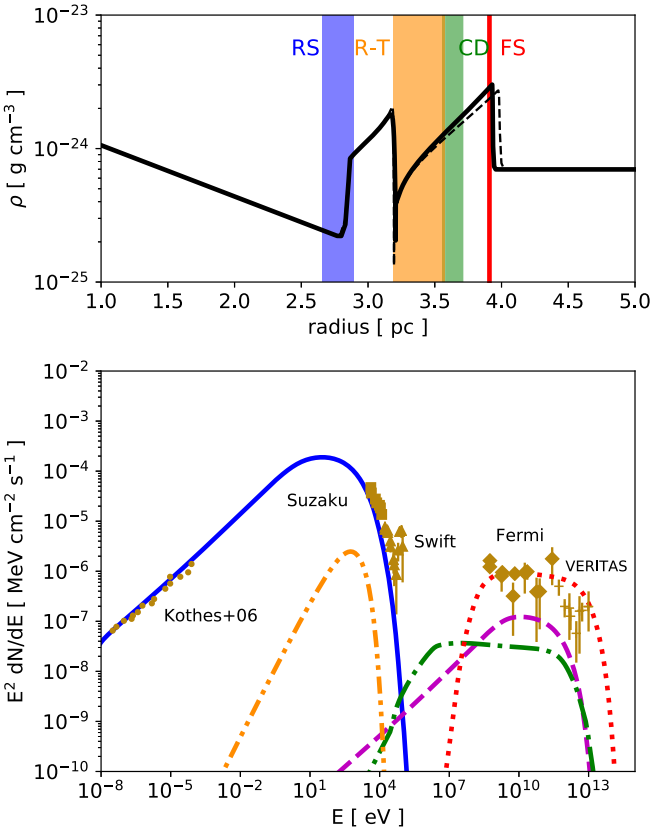

Figure 2. Top panel: the solid line shows the calculated density distribution from model A0 at an age of 446 yr. The color bands show the observed ranges of FS (red), CD (green), and RS (blue) radii of Tycho's SNR taken from Warren et al. (2005). The orange band indicates the extent of expected R-T mixing (Wang & Chevalier 2001). The dashed line is the result from an identical model but without including CR feedback. Bottom panel: corresponding calculated nonthermal SED decomposed into its individual emission components, including synchrotron (blue solid), thermal bremsstrahlung (orange double-dot-dashed), nonthermal bremsstrahlung (green dot-dashed), IC (magenta dashed), and π^0-decay (red dotted). The data points show the currently available observed fluxes—radio observations (Kothes et al. 2006; dotted), X-ray observations by *Suzaku* (Giordano et al. 2012, and references therein; square) and *Swift*/BAT (Troja et al. 2014; triangle), and γ-ray observations by *Fermi*-LAT (Giordano et al. 2012; Archambault et al. 2017; rhombus) and *VERITAS* (Acciari et al. 2011; Archambault et al. 2017; cross).

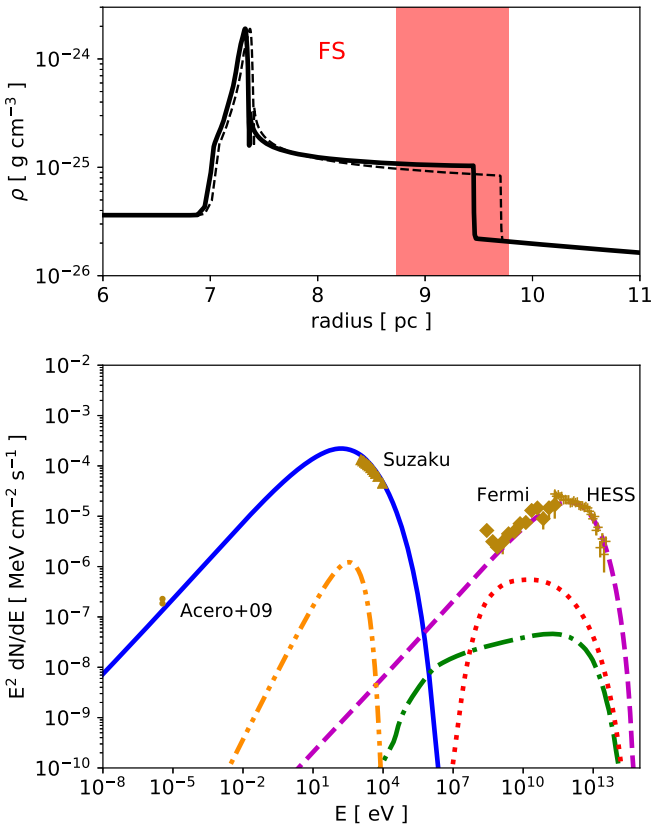

Figure 3. Results from model B0. The format is the same as in Figure 2. A normalization factor $f_{\rm norm} = 0.7$ has been applied to all calculated emission components to match the observed flux. Data points in bottom panel: radio observations (Acero et al. 2009; dotted), X-ray observation by *Suzaku* (Lazendic et al. 2004; triangle), γ-ray observation by *Fermi*-LAT (Aharonian et al. 2007, 2011; H.E.S.S. Collaboration et al. 2018a; diamond) and H.E.S.S. (H.E.S.S. Collaboration et al. 2018a; cross).

spectrum from *Fermi* and *VERITAS* data, which can be explained by a π^0-decay origin with a softer-than-E^{-2} underlying proton spectrum, but the mechanism of spectral softening of the accelerated protons relative to the canonical E^{-2} prediction of DSA at a strong shock is not yet well understood.

RX J1713 is believed to be the product of SN 393, which has been classified as a CCSN, and the SNR has been well detected in multiwavelength observations. The origin of the bright γ-ray emission from RX J1713 is still being intensively discussed as mentioned above. Fukui et al. (2012) reported that the azimuthal distributions of H I and H_2 gases are consistent with the morphology of the observed TeV γ-rays, suggesting a hadronic origin. The gas distribution exhibits a low-density cavity surrounded by a dense shell, which has been suggested to be the result of the stellar wind of the progenitor prior to SN explosion inside a dense gas cloud. One the other hand, the observed hard γ-ray spectrum and the absence of optical signatures of the shock interacting with dense gas support a leptonic origin. In model B0, we adopt a simple power-law $\rho \propto r^{-2}$ CSM model without considering the possibility of shock–cloud interaction, which is similar to the best-fit model for RX J1713 presented in Lee et al. (2012). The results are summarized in Figure 3, which shows the time snapshots of the gas density profile and emission SED at $t_{\rm age} = 1625$ yr. The FS position observed by *Fermi*-LAT (Acero et al. 2016) is shown by the red shaded region in the top panel, which is consistent with the model. The CD and RS locations for this remnant are not well constrained owing to the very faint X-ray emission from the ejecta. The radio and nonthermal X-ray spectra can be well reproduced by the model, and the hard observed γ-ray spectrum is well reproduced by an IC origin. The results are found to be consistent with the model by Lee et al. (2012).

Our result that the γ-ray emission is dominated by the IC component can be understood by considering the spatial distribution of the ambient gas density and magnetic field. The global magnetic field B_0 is as low as $\sim 6.6 \times 10^{-2}$ $(\sigma_{\rm w}/0.004)^{1/2}$ $(\dot{M}/7.5 \times 10^{-6}\ M_\odot\ {\rm yr}^{-1})^{1/2}$ $(V_{\rm w}/20\ {\rm km\ s}^{-1})^{1/2}$ $(r/9.5\ {\rm pc})^{-1}$ μG at $t_{\rm age} = 1625$ yr, so the amplified magnetic field B_2 is also moderate, $\sim 6.4\ \mu$G, at the same time. This amplified but relatively low B-field behind the shock leads to an inefficient synchrotron loss such that the electrons can be accelerated to momenta capable of powering the observed γ-rays through the IC mechanism. Meanwhile, the ambient gas density also decreases rapidly as the SNR expands into the wind, so that the π^0 decay component is effectively suppressed.

We also note that we applied a flux normalization factor, $f_{\rm norm} = 0.7$, for all calculated emissions to match the

Table 1
SED References

SNR	Radio	X-Ray	GeV γ-Ray	TeV γ-Ray
G34.7−0.4	⋯	⋯	Ackermann et al. (2013) Giuliani et al. (2011)	⋯
G111.7−2.1	Artyukh et al. (1967)	Maeda et al. (2009) Wang & Li (2016)	Abdo et al. (2010)	Acciari et al. (2010) Sinitsina & Sinitsina (2015) Ahnen et al. (2017)
G120.1+1.4	Kothes et al. (2006)	Troja et al. (2014)	Giordano et al. (2012) Archambault et al. (2017)	Acciari et al. (2011) Archambault et al. (2017)
G189.1+3.0			Tavani et al. (2010) Ackermann et al. (2013)	Albert et al. (2007) Acciari et al. (2009)
G260.4−3.4	Hewitt et al. (2012) Planck Collaboration et al. (2016)		Xin et al. (2017)	H.E.S.S. Collaboration et al. (2015)
G266.2−1.2	Duncan & Green (2000)		Tanaka et al. (2011)	H.E.S.S. Collaboration et al. (2018b)
G327.6+14.6	Allen et al. (2001)	Bamba et al. (2008)	Condon et al. (2017)	Acero et al. (2010)
G347.3−0.5	Lazendic et al. (2004) Acero et al. (2009)	Tanaka et al. (2008)	Abdo et al. (2011)	Aharonian et al. (2007) Aharonian et al. (2011) H.E.S.S. Collaboration et al. (2018a)

Note. The SED data references in each wavelength in Figures 1–3.

Table 2
Model Parameters

Model	$M_{\rm ej}$ ($M_\odot$)	$n_{\rm ISM}$ (cm^{-3})	$\dot{M}$ ($M_\odot$ yr^{-1})	$V_{\rm w}$ (km s^{-1})	$\dot{M}_2$ ($M_\odot$ yr^{-1})	$V_{\rm w,2}$ (km s^{-1})	$\chi_{\rm inj}$
A0[a]	1.4	0.3	⋯	⋯	⋯	⋯	3.6
A1	1.4	0.01	⋯	⋯	⋯	⋯	3.6
A2	1.4	0.1	⋯	⋯	⋯	⋯	3.6
A3	1.4	1.0	⋯	⋯	⋯	⋯	3.6
B0[b]	3.0	⋯	7.5×10^{-6}	20	⋯	⋯	3.75
B1	3.0	⋯	1.0×10^{-6}	20	⋯	⋯	3.75
B2	3.0	⋯	1.0×10^{-5}	20	⋯	⋯	3.75
B3	3.0	⋯	1.0×10^{-4}	20	⋯	⋯	3.75
B4	10.0	⋯	1.0×10^{-6}	20	⋯	⋯	3.75
B5	10.0	⋯	1.0×10^{-5}	20	⋯	⋯	3.75
B6	10.0	⋯	1.0×10^{-4}	20	⋯	⋯	3.75
C[c]	10.0	⋯	5.0×10^{-6}	15	0.01	1000	3.75

Notes.
[a] All elements of model A use an exponential profile for the ejecta, $E_{\rm SN} = 10^{51}$ erg, $T_0 = 10^4$ K, $B_0 = 4.0$ μG, and $d_{\rm SNR} = 3.2$ kpc.
[b] All elements of model B use a power-law profile for the ejecta with $n_{\rm pl} = 7$, $E_{\rm SN} = 10^{51}$ erg, $T_0 = 10^4$ K, $\sigma_{\rm w} = 0.004$, and $d_{\rm SNR} = 1.0$ kpc.
[c] This model uses a power-law profile for the ejecta with $n_{\rm pl} = 7$, $E_{\rm SN} = 10^{51}$ erg, $T_0 = 10^4$ K, $n_{\rm pl,2} = 1.5$, and $d_{\rm SNR} = 1.0$ kpc.

observations, mainly for two reasons: the distance of the SNR and a volume filling factor. We assume 1.0 kpc as the distance of RX J1713 in this work, which involves uncertainty. While our models assume spherically symmetry, many SNRs like RX J1713 are not a perfect spherical shell in gamma-rays (see, e.g., Figure 1(a) in Fukui et al. 2012). In other words, a prefactor <1 has to be applied to our spectral SED to account for this volume filling factor. These uncertainties can be interpreted as the possible origins of $f_{\rm norm}$ in our models.

Based on our calibrated models A0 and B0 for a Type Ia and a CC SNR, respectively, we now parametrically study the time evolution of broadband nonthermal SED from SNRs interacting with different ambient environments. We note that we have chosen an ejecta mass of $M_{\rm ej} = 3.0\,M_\odot$ to calibrate with RX J1713 in model B0, but the ejecta mass can vary for different CCSN progenitors and SN types (e.g., Nicholl et al. 2015). Therefore, for model B with a power-law CSM environment, we will survey over two ejecta models with $M_{\rm ej} = 3.0$, 10.0 $M_\odot$, respectively. Other parameters are kept identical to models A0 and B0 unless otherwise specified. The model parameters are summarized in Table 2.

3.2. Type Ia SNR Models with a Uniform ISM-like Ambient Medium

The left panel of Figure 4 shows the time evolution of the broadband SED from our Type Ia SNR models A1, A2, and A3 for three different ISM densities, and the right panel shows the

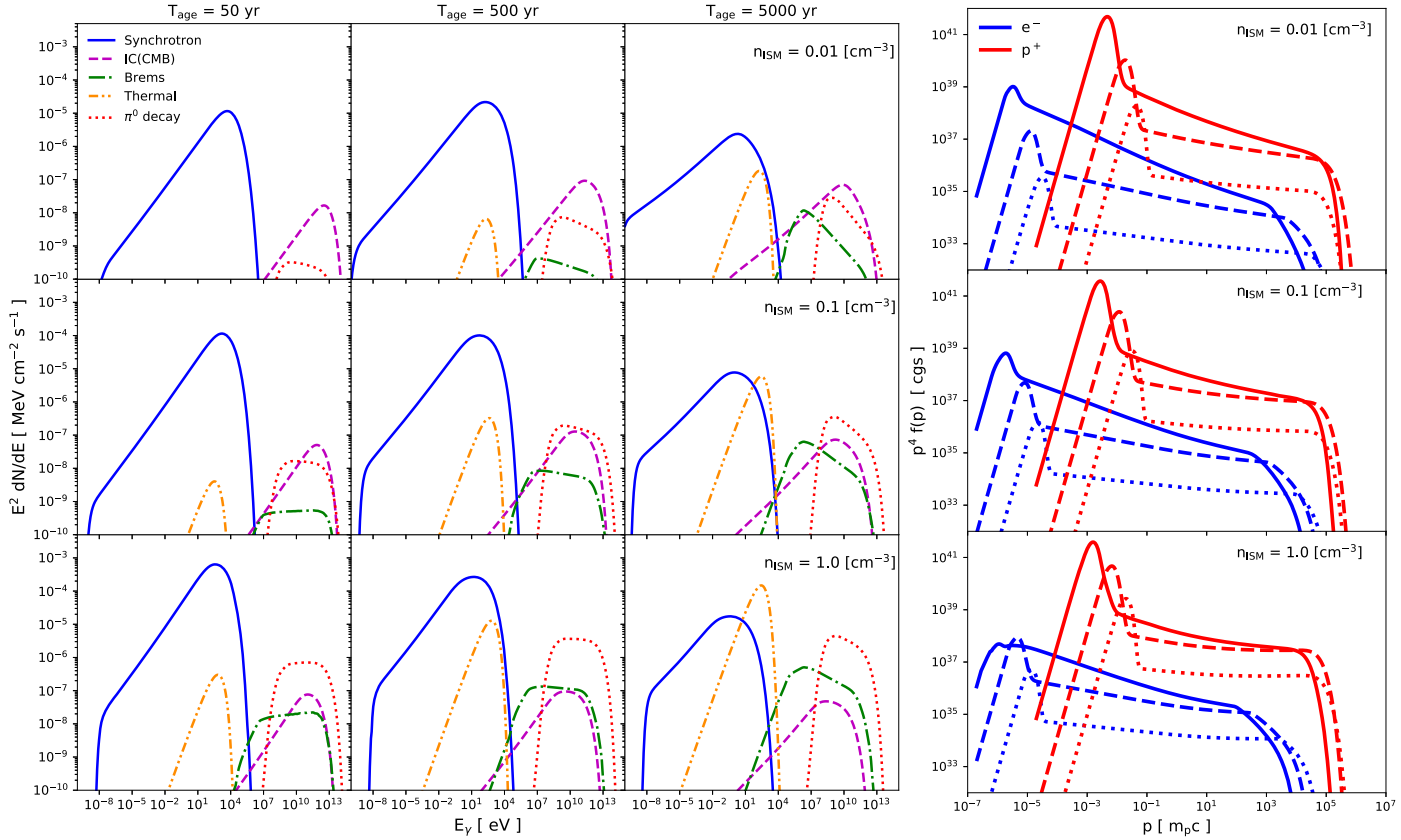

Figure 4. Left panel: time evolution of volume-integrated broadband SED from Type Ia SNR models with different ISM densities. Here $t_{\rm age} = 50$, 500, and 5000 yr moving from left to right panels, and $n_{\rm ISM} = 0.01$, 0.1, and 1.0 cm^{-3} from top to bottom, which correspond to models A1, A2, and A3, respectively. The line formats are identical to the bottom panel of Figure 2 and Figure 3. Right panel: time evolution of volume-integrated proton (red) and electron (blue) distribution functions with different ISM densities. Here $n_{\rm ISM} = 0.01$, 0.1, and 1.0 cm^{-3} moving from top to bottom, and the dotted, dashed, and solid lines correspond to $t_{\rm age} = 50$, 500, and 5000 yr, respectively.

corresponding evolution of the underlying CR distribution functions. Figure 5 shows the time evolution of important hydrodynamical and DSA outputs. In the GeV-to-TeV energy range, as time evolves, the flux of nonthermal bremsstrahlung (green dot-dashed line) and π^0-decay (red dotted line) are found to be increasing monotonically, but there is not much accompanied brightening in the IC component (magenta dashed line). This difference in the evolution is mainly caused by the energy loss of the accelerated particles. The intensities of nonthermal bremsstrahlung, π^0-decay, and IC are proportional to the fluxes of the accelerated particles multiplied by the number density of their respective interaction targets, i.e., ISM gas for nonthermal bremsstrahlung and π^0-decay, and CMB photons for IC. However, the high-energy flux of the accelerated electrons is highly suppressed by a fast energy loss owing to synchrotron radiation. The synchrotron loss timescale, $t_{\rm syn} = 3m_e c^2/4c\sigma_{\rm T} U_{\rm B}\gamma \sim 130(E_e/10\ {\rm TeV})^{-1}\ (B/100\ \mu{\rm G})^{-2}$ yr, is comparable to the SNR age, with the post-shock magnetic field $\sim$100 μG being highly amplified in the shock precursor relative to the unshocked magnetic field $B_0 = 4.0$ μG owing to an efficient CR acceleration (see panels (c) and (e) of Figure 5). On the other hand, although the proton spectrum also suffers from energy loss from p–p inelastic scatterings, even in the denser case of $n_{\rm ISM} = 1.0$ cm^{-3}, the energy-loss timescale $t_{\rm pp} = 1/\sigma_{\rm pp} v_{\rm p} n_{\rm SNR} \sim 3 \times 10^7 R_{\rm tot}^{-1} (n_{\rm ISM}/1\ {\rm cm}^3)^{-1}$ yr is still much longer than the SNR age, so the effect is not significant on the protons. As a result, the peak of the IC spectrum shifts to lower energy in the early phase owing to the fast synchrotron loss, and the peak flux does not vary much as the SNR ages.

From the trend of flux evolution, we can see an interesting *leptonic*-to-*hadronic* transition in the moderately dense ISM case $n_{\rm ISM} = 0.1$ cm^{-3} at a few $\times$ 10^2 yr. The middle panels in Figure 4 show that the dominant flux of the TeV range is IC at $t_{\rm age} = 50$ yr, while π^0 flux becomes comparable to IC at $t_{\rm age} = 500$ yr, and finally π^0 surpasses IC at $t_{\rm age} = 5000$ yr. On the other hand, in the thin and dense ISM cases, the transition does not happen within a few $\times$ 10^3 yr. This behavior is mainly dictated by the gas density interacting with the shock (see the top and bottom panels of Figure 4).

We also see a systematic steepening of the γ-ray spectra with age in all models, which reflects the steeping of the proton spectrum from Equation (3). This effect comes from the deceleration of the FS with time due to an asymptote from free-expansion phase to Sedov phase. As a result, v_A, which is high owing to the amplified B-field, becomes non-negligible compared to the gas velocities in the later phase, and the effective compression ratio $S_{\rm tot}$ is suppressed. The γ-ray spectrum hence becomes steeper with time because the spectral index of the particle distribution function is roughly proportional to $3S_{\rm tot}/(S_{\rm tot} - 1)$ (Caprioli et al. 2009b). The steepening is even more prominent in the thin ISM case since $v_A \propto \rho^{-1/2}$ is larger in these models.

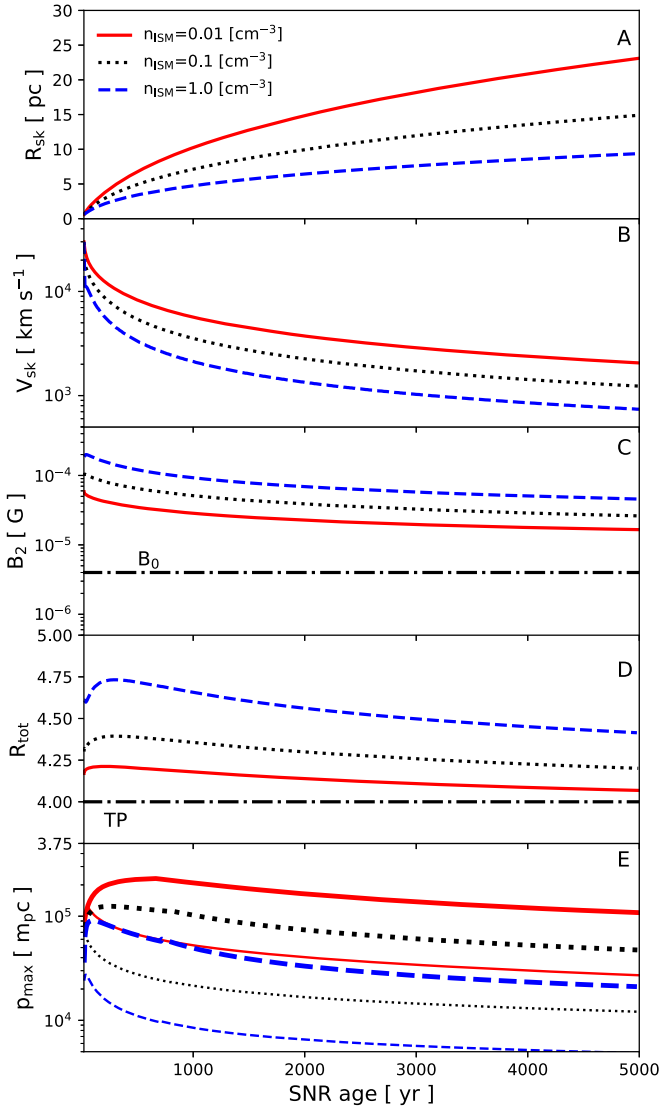

Figure 5. Time evolution of hydro and DSA outputs from our Type Ia models A1, A2, and A3 in three different ISM densities. Panel (a) shows the forward shock radius $R_{\rm sk}$, panel (b) shows the forward shock velocity $V_{\rm sk}$, panel (c) shows the magnetic field strength immediately downstream from the forward shock, panel (d) shows the total shock compression ratio, and panel (e) shows the maximum momentum $p_{\rm max}$ of accelerated protons (thick lines) and electrons (thin lines). In all panels, the red solid, black dotted, and blue dashed lines correspond to the cases of $n_{\rm ISM} = 0.\ 01$, 0.1, and 1.0 cm^{-3}, respectively. The dot-dashed line shows the value of the ambient magnetic field $B_0 = 4.0$ μG in panel (c) and the expected compression ratio from a test-particle (TP) approximation $R_{\rm tot} = 4$ in panel (d).

3.3. CC SNR Models with a Power-law CSM-like Ambient Medium

3.3.1. 3 $M_\odot$ Case

Here we simulate the SNR evolution in a power-law CSM inside which a CCSN explodes with an ejecta mass of $M_{\rm ej} = 3.0\ M_\odot$. The results are shown in Figures 6 and 7. The models correspond to a CSM with $\dot{M} = 10^{-6}$, 10^{-5}, and $10^{-4}\ M_\odot$ yr^{-1} for models B1, B2, and B3, respectively. In the GeV–TeV spectrum, the IC flux increases, while the π^0-decay and nonthermal bremsstrahlung fluxes decrease as time proceeds, which is the opposite behavior compared to the uniform ISM models we see earlier. Since the CSM has a power-law density distribution in these CC SNR models, the CSM provides a dense target for producing π^0-decay and bremsstrahlung photons effectively, which dominate the spectrum in the GeV–TeV range in the very early phase after the explosion. However, as the CSM density decreases as r^{-2}, as time passes and the shock propagates through the wind material, the target gas density becomes low quickly, so the emission efficiency through π^0-decay and bremsstrahlung is suppressed accordingly. Moreover, the accelerated particles advected downstream from the shock also suffer from adiabatic loss to a larger extent than model A owing to the fast expansion of the SNR in a $\rho \propto r^{-2}$ wind. As a result, the fluxes of π^0-decay and nonthermal bremsstrahlung constantly decrease with age. On the contrary, the target photons of IC, which is CMB here, are homogeneous in space. The magnetic field is also lower than those we see in the uniform ISM cases (see panel (c) of Figure 5 compared to that of Figure 7). This means that synchrotron loss is less important in the CC SNR models. Indeed, the quick shift of the peak energy of the synchrotron and IC components that is seen in Figure 4 does not occur here, and the IC emission gradually increases with time, with the peak staying at more or less the same energy range. These are the main reasons why the IC photons are constantly produced in the power-law CSM cases. In the middle and bottom panels of Figure 6, we can also see a low-energy cutoff in the synchrotron spectrum in the radio band. This is because free–free absorption is efficient at early time owing to the dense unshocked CSM in front of the shock. The absorption becomes inefficient with time, however, as the SNR shock propagates into the relatively thin region of the CSM, and so the cutoff shifts to lower frequencies.

Our SED evolution model for the CCSN with power-law CSM cases suggests a *hadronic*-to-*leptonic* transition in the GeV–TeV range if the wind density is moderately dense with an $\dot{M} = 10^{-5}\ M_\odot$ yr^{-1}, which is again the exact opposite behavior we see in the Type Ia SN cases with uniform ISM. We suggest that the contrasting spectral evolution and transition of the dominant γ-ray component can be useful for probing the surrounding environment of SNRs, especially in the near future as the sample of γ-ray SNR observations is enlarged by future observatories such as CTA (see Section 3.6).

3.3.2. 10 $M_\odot$ Case

The results from our CCSN models with an ejecta mass $M_{\rm ej} = 10\ M_\odot$ are shown in Figure 8. For comparison, the results of $M_{\rm ej} = 3\ M_\odot$ are also overlaid. From panels (a) and (b), it can be seen that while the shock dynamics for the case of $\dot{M} = 10^{-6}\ M_\odot$ yr^{-1} and $\dot{M} = 10^{-5}\ M_\odot$ yr^{-1} are affected by a different ejecta mass, the results for $\dot{M} = 10^{-4}\ M_\odot$ yr^{-1} are nearly identical. These differences can be explained by a different evolutionary phase of the SNR at a given age. In the cases of $\dot{M} = 10^{-6}\ M_\odot$ yr^{-1} and $\dot{M} = 10^{-5}\ M_\odot$ yr^{-1}, the CSM density is relatively low and the mass swept up by the FS is smaller than the ejecta mass; the dynamics of these two cases thus follow the self-similar solution, $R_{\rm sk} \propto (E_{\rm SN}/M_{\rm ej}A)^{1/5}t^{4/5}$ and $V_{\rm sk} \propto (E_{\rm SN}/M_{\rm ej}A)^{1/5}t^{-1/5}$ (Chevalier 1982a, 1982b), where $A \equiv \dot{M}/4\pi V_w$, which depends on the ejecta mass. On the contrary, the CSM material in the case of $\dot{M} = 10^{-4}\ M_\odot$ yr^{-1} is dense enough and the swept-up mass becomes comparable to the ejecta mass at $t_{\rm age} \leqslant 1000$ yr; the dynamics hence follows the Sedov solution, $R_{\rm sk} \propto (E_{\rm SN}/A)^{1/3}t^{2/3}$ and

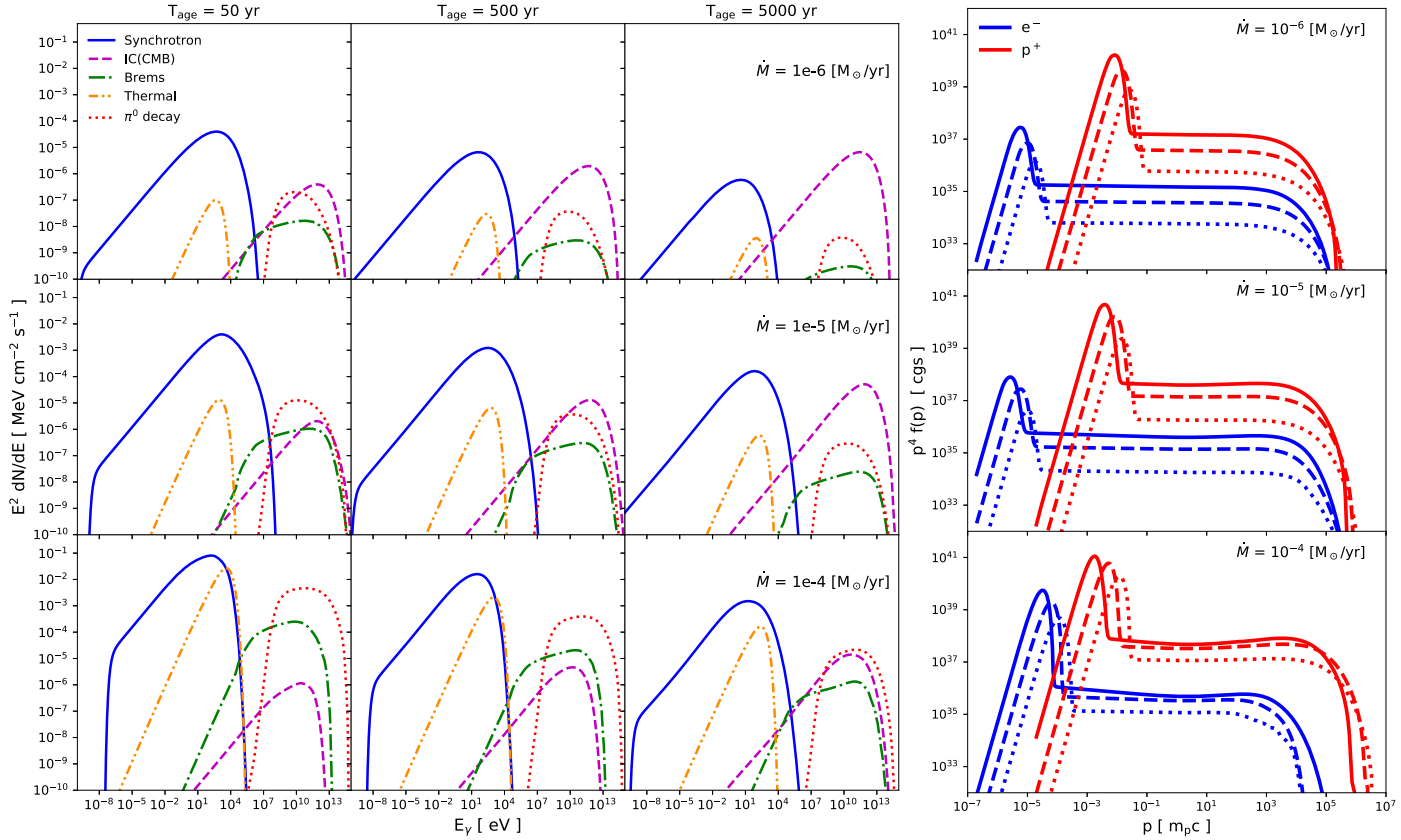

Figure 6. Left panel: SED evolution for our CC SNR models in different CSM environments. $t_{\rm age} = 50$, 500, 5000 yr from left to right and $\dot{M} = 10^{-6}$, 10^{-5}, $10^{-4}\ M_\odot\ {\rm yr}^{-1}$ from top to bottom, which corresponds to models B1, B2, and B3, respectively. The lines shown have the same format as in the left panel of Figure 4. Right panel: time evolution of CR distribution function. $\dot{M} = 10^{-6}$, 10^{-5}, $10^{-4}\ M_\odot\ {\rm yr}^{-1}$ from top to bottom. The lines shown have the same format as in the right panel of Figure 4.

$V_{\rm sk} \propto (E_{\rm SN}/A)^{1/3} t^{-1/3}$ (Sedov 1959), which are independent of the ejecta mass.

As for the other quantities shown in Figure 8 like B-field and $p_{\rm max}$, the differences are found to be subtle only.[4] As a result, we do not see any remarkable difference in the nonthermal SED between the 3 and 10 $M_\odot$ models. We can conclude that it is hard to distinguish the progenitor from the nonthermal emission in the SNR phase, and other information that reflects the progenitor properties, such as thermal X-ray emission lines, is needed to link an observed SNR to its progenitor origin. In Section 3.5, where we compare our results to observations, we will only show the results from the 3 $M_\odot$ models because of this insensitivity of the γ-ray emission to ejecta mass.

3.4. A Case of Pre-SN Enhanced Mass Loss

Results from model C, where the $\dot{M}$ is boosted to $10^{-2}\ M_\odot\ {\rm yr}^{-1}$ in the last 1000 yr before CC, are shown in Figures 9 and 10. Figure 9 shows the phase-space distributions of the accelerated primary (solid) and secondary (dashed) particles in the top panels and the photon SEDs in the bottom panels. We choose to show the results at $t_{\rm age} = 400$ yr (left panels) and 1000 yr (right panels) because these time epochs represent the phases before and after the shock has crossed the interface at $R_{\rm tr}$ between the dense confined CSM and the less dense wind outside. In this model, the shock reaches $R_{\rm tr}$ at $t_{\rm age} \sim 600$ yr (see Figure 10).

As the FS propagates in the region of dense CSM material with density $n \sim 10^4\ {\rm cm}^{-3}$ and a high magnetic field $\geqslant 1$ mG (see panel (c) of Figure 10), the electron maximum momentum $p_{\rm max,e}$ is determined by the energy-loss timescale $t_{\rm loss}$ rather than the age or escape timescale because $t_{\rm loss} \sim t_{\rm syn} \sim 12 B_{-3}^{-2} E_{12}^{-1}$ yr, where $B_{-3} = B_2/10^{-3}$ G and $E_{12} = E_e/10^{12}$ eV, is less than the SNR age at a given time (see panel (e) of Figure 10). However, as the FS breaks out from the dense inner shell, $p_{\rm max,\,e}$ is now limited by their escape through the FEB because the shock velocity is now restored to $\sim$4000 km s^{-1} and the magnetic field decreases to $\sim 10\ \mu$G (see panels (b), (c), and (e) of Figure 10). Therefore, we can see two cutoffs at $p \sim 10\ m_{\rm p}c$ and $p \sim 10^3\ m_{\rm p}c$ in the volume-integrated electron spectrum (top right panel of Figure 9), while the proton spectrum has one cutoff only at $p \sim 10^4 m_{\rm p}c$. These effects of a transition from a dense wind to a lower-density wind also reflect in the spectra of synchrotron, nonthermal bremsstrahlung, and IC emission (see bottom right panel of Figure 9).

In the radio range of the SED, before the shock breaks out from the dense region, the dominant component is synchrotron radiation from the primary electrons (solid), and a spectral cutoff can be seen at $E_\gamma \sim 10^{-7}$ eV owing to a strong free–free absorption. However, after the breakout, the dominant component is now the synchrotron emission from the secondary electrons and positrons. The reason is as follows. Electrons accelerated earlier on in the dense wind suffer from rapid energy loss through

[4] The fact that the shock velocities in the 10 $M_\odot$ cases are lower than those of the 3 $M_\odot$ models at any given age implies that the effects of CR back-reaction and shock modification become important at an earlier phase. This is evident from the slightly higher total compression ratio and amplified magnetic field, as shown in panels (c) and (d) of Figure 8.

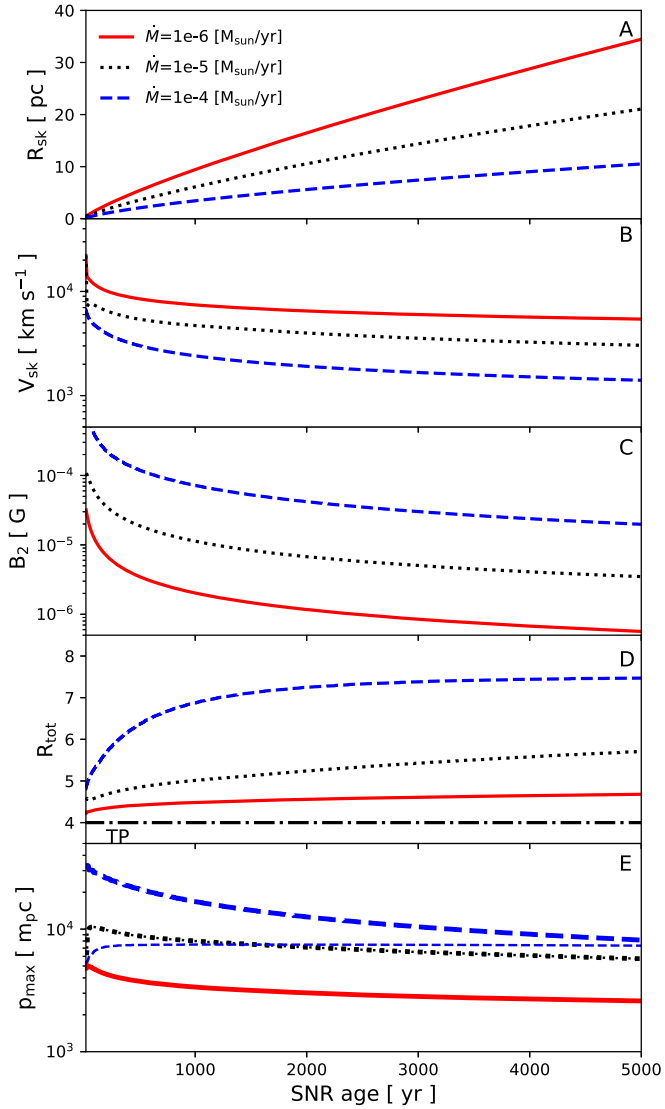

Figure 7. Time evolution of hydro and DSA outputs from models B1, B2, and B3. In all panels, the red solid, black dotted, and blue dashed lines correspond to the cases of $\dot{M} = 10^{-6}$, 10^{-5}, 10^{-4} $M_\odot$ yr^{-1} respectively. The line formats are identical to Figure 5.

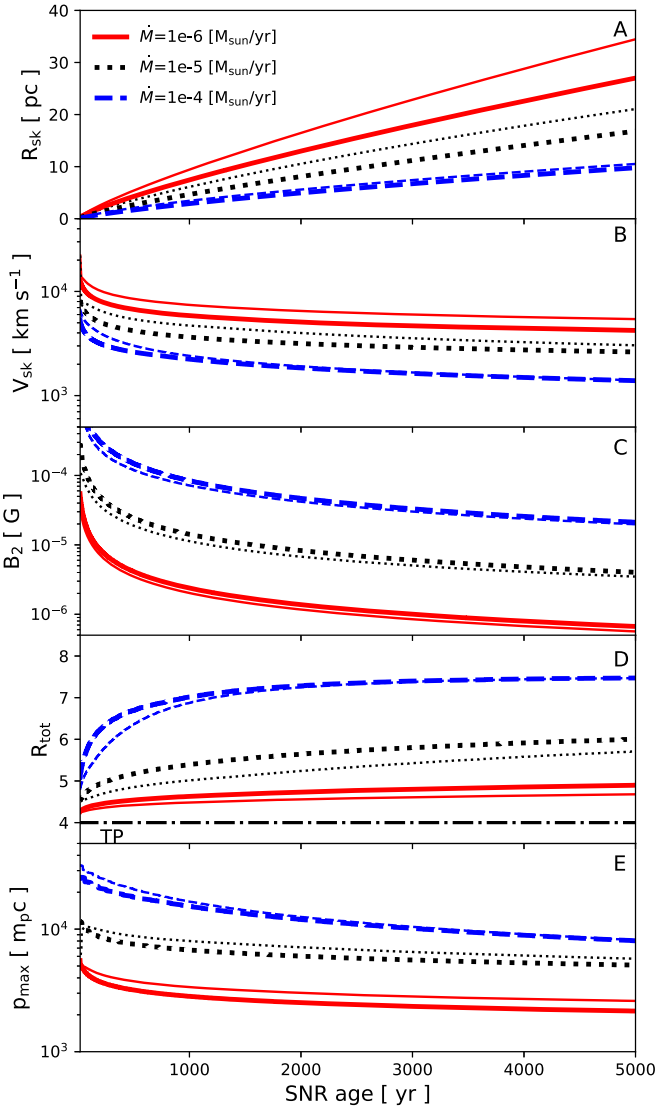

Figure 8. Same as Figure 7, but with an ejecta mass of $M_{ej} = 10.0\ M_\odot$. Only the p_{max} of protons is plotted here in panel (e) for clarity. The thick red solid, black dotted, and blue dashed lines show the results of models B4, B5, and B6, respectively. For comparison, thin lines show the results of the 3 $M_\odot$ case as in Figure 7.

synchrotron emission and adiabatic expansion, and the freshly accelerated electrons in the outer tenuous wind have a higher p_{max} as mentioned above, but the synchrotron radiation from these freshly accelerated electrons is relatively weak owing to a lower magnetic field in the tenuous wind; therefore, the synchrotron flux from the primaries decreases with time. On the other hand, the contribution from the secondaries does not decrease as rapidly because these secondary particles are produced via π^0-decay not only by the freshly accelerated protons but also by the protons accelerated earlier on in the dense wind continuously, as the protons do not lose their energy as quickly as the electrons. This is why the transition from primary to secondary dominance happens in the synchrotron radiation.

We suggest that this transition can potentially constrain the mass-loss history of massive stars. For example, the spectral index of synchrotron emission produced by the secondary particles is expected to be different from that produced by the primary electrons, which is evident from their very different distribution functions as shown in the top panels of Figure 9. In particular, the synchrotron spectrum from the secondaries tends to be harder in the radio band. In fact, hard radio indices are usually observed in older SNRs interacting with dense molecular clouds, such as IC 443 (e.g., Castelletti et al. 2007, 2011). These remnants are also believed to be producing a significant amount of secondaries. If a harder-than-expected spectral index will be observed in a young SNR that is not colliding with any dense cloud at the moment, it is possible that the SNR has evolved inside a dense confined CSM in the past, which can provide a hint on the enhanced mass loss of the progenitor star prior to CC.

3.5. Model versus Data

We now try to compare our simulation results to observation results so far in terms of dynamics (e.g., shock radius and velocity) and γ-ray luminosity to check if our models are able to reproduce the bulk properties of observed SNRs. We include

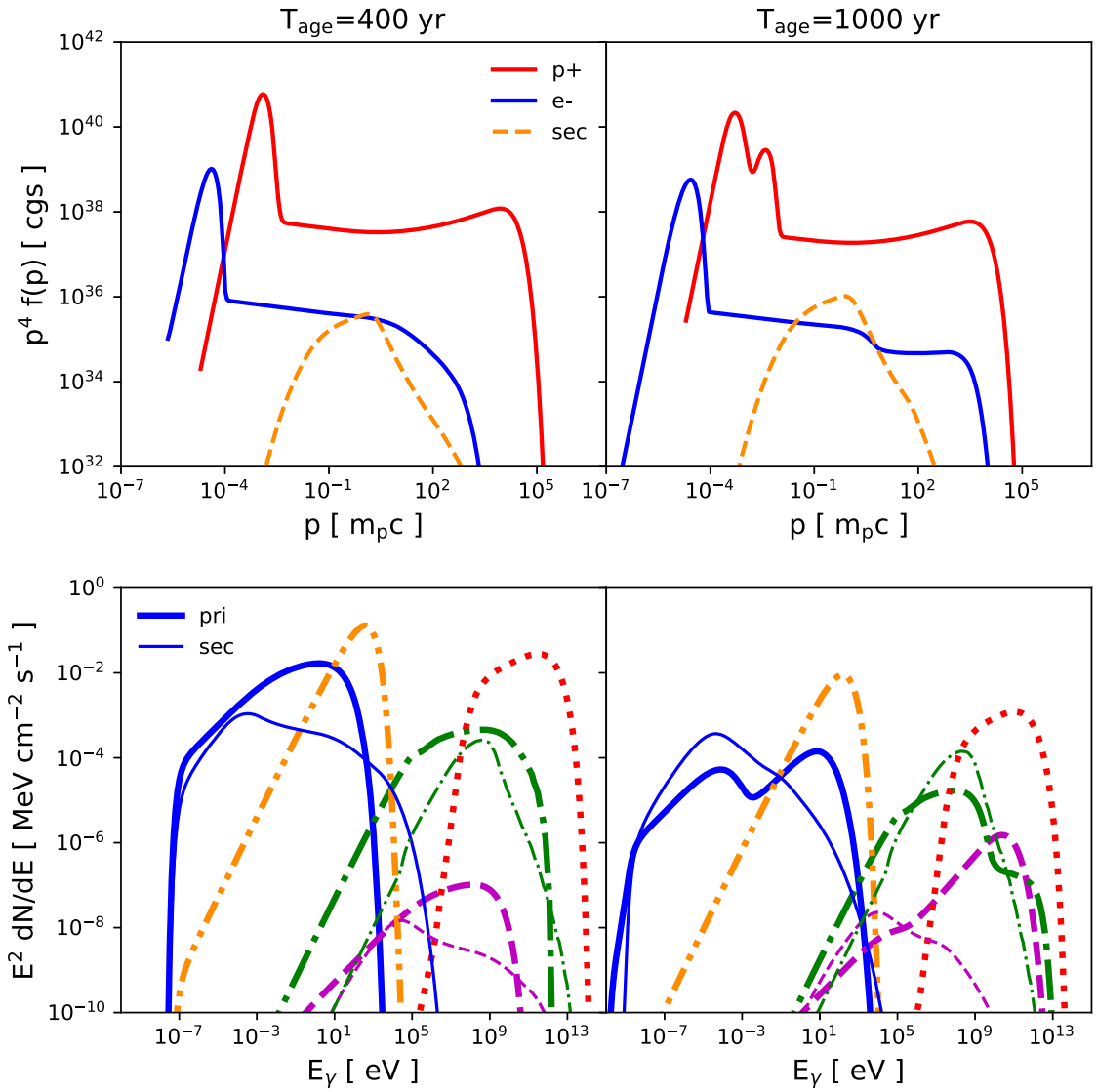

Figure 9. Time evolution of the volume-integrated distribution function of the accelerated particles (top panels) and broadband emission SED (bottom panels), which correspond to model C. Left and right panels show the results at $t_{age} = 400$ and 1000 yr, respectively. In the top panels, the red solid, blue solid, and orange dashed lines correspond to the primary protons, electrons, and secondary electrons/positrons, respectively. In the bottom panels, the thick lines show the emission produced by the primary particles, and the thin lines are by the secondaries. The line colors are the same as in Figure 4.

data like SN type, distance, shock radius, shock velocity, and radio, GeV, and TeV fluxes of SNRs from a younger age (∼100 yr) to middle age (∼10,000 yr). We summarize these data in Table 3. The data on SNR radii with errors are taken from the *Fermi* catalog (Acero et al. 2016), and those without errors are determined by the size of the radio remnants and are taken from the *SNRcat* (Ferrand & Safi-Harb 2012). The flux data are obtained again mainly from the *Fermi* and H.E.S.S (H.E.S.S. Collaboration et al. 2018a) catalogs (see Table 3 for details); those with errors are for detected SNRs, and those without errors are the upper limits of nondetected SNRs.

Figure 11 shows the comparison of dynamical properties, including the shock radius and shock velocity, as a function of time from our models with observations. The blue data points are for the Type Ia SNRs, and red ones are for the CC SNRs. We label each SNR by a number as summarized in the left panel of Figure 11. In general, the overall trend of the observed distribution of shock radius and velocity as a function of SNR age can be explained by our simulation results for the parameter space we explored. There exist a few "outliers" that have small radii and velocities, which can be interpreted as SNRs interacting with a medium denser than what our models have considered. In fact, many of these are known to be interacting with dense molecular clouds at the moment.

Figure 12 shows the time evolution of the luminosity in three different energy ranges. The top left panel shows the luminosity of 1 GHz radio continuum emission, which reflects the time evolution of synchrotron spectrum for both the uniform ISM cases and power-law CSM cases (see also Figures 4 and 6). Since synchrotron emissivity is proportional to the flux of accelerated electrons and the square of the local magnetic field strength, for the magnetic field that is constantly distributed in the uniform ISM cases, the synchrotron emissivity does not vary much and the spectral peak shifts to a lower energy with time, similar to the IC component previously discussed in Section 3.2. On the other hand, in a power-law CSM case, the magnetic field decreases in proportion to r^{-1}, and the synchrotron flux then also decreases

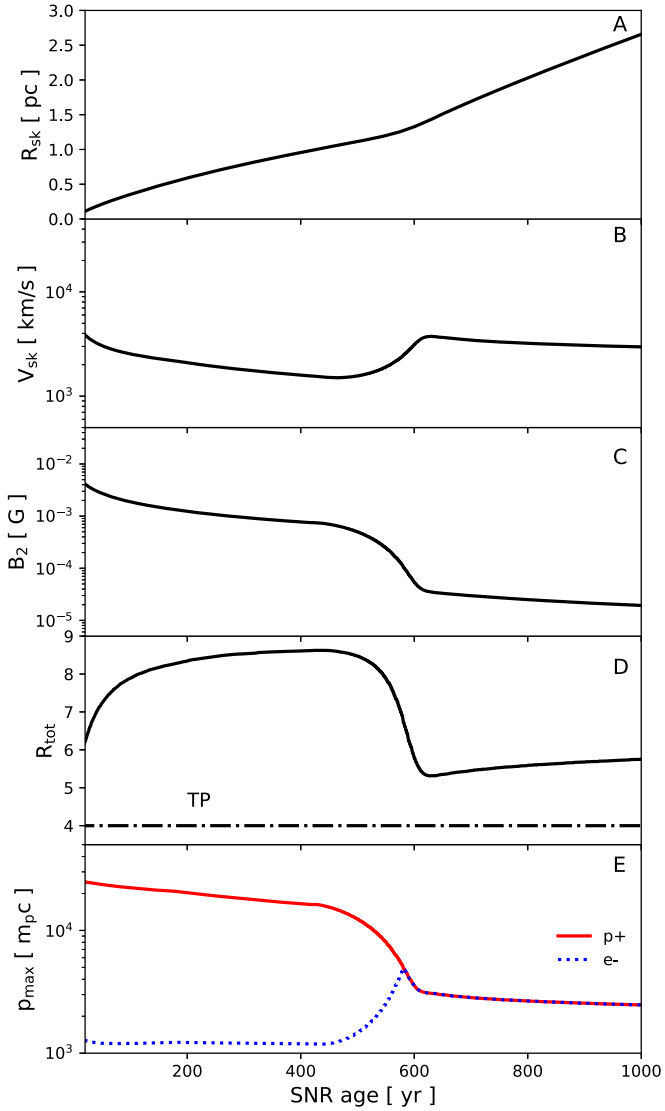

Figure 10. Time evolution of various values using model C. The values of each panel are the same as in Figures 5 and 7.

with time just as the π^0-decay γ-rays do. Thus, radio luminosity increases gradually with time as a volume effect in the uniform ISM cases but decreases in the power-law CSM cases.

The top right and bottom left panels show the GeV luminosity integrated from 1 to 100 GeV and TeV luminosity from 1 to 10 TeV as a function of age, respectively. For the uniform ISM cases, while the GeV luminosity increases with time, TeV luminosity decreases. At the bottom end of the predicted flux, which corresponds to the case of $n_{\rm ISM} = 0.01\,{\rm cm}^{-3}$, the γ-rays are dominated by IC at all times, and the decrease of the TeV flux can be understood as the energy loss of the highest-energy electrons. For the other two cases with a denser ISM, the trend reflects the time evolution of not only the normalization but also the shape of the π^0-decay spectra predicted by these models. As seen in Figure 4, the π^0-decay spectrum becomes softer as time passes by. The reason has been discussed in the end of Section 3.2, which is mainly because of the increasing importance of the effect from v_A, i.e., the velocity of the magnetic scattering centers. As the shock sweeps up more material as the SNR ages, the π^0-decay flux increases with time in general, but the TeV flux decreases owing to a spectral softening of the underlying proton distribution.

On the other hand, in the power-law CSM cases, both GeV and TeV luminosities decrease only in the case of the densest wind with $\dot{M} = 10^{-4} M_\odot\ {\rm yr}^{-1}$, but they increase in the other two cases. This can be easily understood according to the discussion above in Section 6 on the evolution of IC and π^0-decay fluxes, and the dominant component is π^0-decay in the case of $\dot{M} = 10^{-4} M_\odot\ {\rm yr}^{-1}$.

Here, to obtain the data points from the γ-ray observations, we assume that the observed spectra have a simple power-law distribution, so that the integrated luminosity can be calculated using the following expression:

$$L_\Delta = 4\pi d_{\rm SNR}^2 \frac{(-\Gamma+1)(E_{\rm max}^{-\Gamma+2} - E_{\rm min}^{-\Gamma+2})}{(-\Gamma+2)(E_{\rm max}^{-\Gamma+1} - E_{\rm min}^{-\Gamma+1})} F_\Delta, \qquad (12)$$

where F_Δ, Γ, $d_{\rm SNR}$, $E_{\rm min}$, $E_{\rm max}$ are the integrated flux, photon index, distance to the SNR, and minimum and maximum energies of the integrated energy range.

The radio luminosities from observations of both Type Ia and CC SNRs can be bulkily reproduced by our models with a few outliers such as Cas A and middle-aged SNRs interacting with MCs. As for the GeV and TeV observations, the statistics is still clearly very poor owing to the small sample size of detected sources, so at the moment the comparison with the models is only preliminary. For older CC SNRs, a few outliers are found with significantly higher luminosities than our results. These are again mostly middle-aged SNRs interacting with dense MCs that are not covered by our parameter space.

The bottom right panel shows the ratio of GeV to TeV luminosities, which roughly quantifies the γ-ray spectral shape. Two trends can be seen in the result: one trend rises with time, and the other is nearly flat. These can be possibly explained by our discussion on flux evolution above. If π^0-decay is the dominant emission in γ-rays, the GeV luminosity increases and TeV luminosity decreases with time in uniform ISM cases, and as a result, the ratio increases with time, while the ratio in the power-law CSM case becomes nearly flat regardless of time because both GeV and TeV luminosities decrease with time and case. If, however, IC is the dominant contributor, the SED evolves without changing its shape, so the ratio does not vary in any significant way with time. Indeed, the observation data also appear to split into two regions, $L_{\rm GeV}/L_{\rm TeV} \sim 1$ and $L_{\rm GeV}/L_{\rm TeV} \geqslant 10$, despite the poor statistics. If both GeV and TeV emissions can be observed from an increased number of SNRs in the future, we will be able to see whether the SNRs will segregate into two groups in this plot, which can make this quantity a useful probe of the ambient environment and hence the progenitor origin of SNRs.

3.6. Prospects for CTA

An instrument that can observe over a broad energy range from GeV to TeV energies with a high sensitivity, such as CTA, is ideal for a systematic investigation as introduced in this study. CTA can achieve an unprecedented sensitivity superior to existing detectors in the 20 GeV–100 TeV energy range. With CTA, we expect that the number of detected γ-ray-emitting SNRs will increase by roughly a factor of 10, which is essential for understanding the SNR population and their ambient environments.

Table 3
Observation Data

SNR	Common Name	Type[a]	Age (yr)	Distance (kpc)	Radius (deg)	Velocity ($''$/yr)	$F_{1\ \mathrm{GHz}}$ (Jy)	$F_{1-100\ \mathrm{GeV}}$[b] (10^{-9} cm^{-2} s^{-1})	$F_{1-10\ \mathrm{TeV}}$[c] (10^{-13} cm^{-2} s^{-1})	References
G1.9+0.3		Ia	150–220	8.5	0.01	0.32 ± 0.02	0.6	0.27	0.72	(1)
G4.5+6.8	*Kepler*	Ia	414	2.9–4.9	0.03	0.23 ± 0.01	19	0.65	0.12	(2)
G15.9+0.2		CC	1000–3000	8.5	0.05	0.021 ± 0.001	5.0	1.6	2.6	(3)
G34.7−0.4	W44	CC	7900–8900	2.7–3.3	0.31 ± 0.02	0.047	240	54.95 ± 2.68	11.2	(4)
G43.3−0.2	W49B	CC	2900–6000	10.9–11.7	0.07	0.022	38	19.24 ± 1.01	⋯	(5)
G67.7+1.8		CC	5000–13000	7.0–17.0	0.11	⋯	1.0	0.43	15.3	(6)
G111.7−2.1	Cas A	CC	316–352	3.3–3.7	0.041 ± 0.001	0.31 ± 0.02	2400	6.25 ± 0.42	5.8 ± 1.2	(7)
G120.1+1.4	Tycho, SN 1572	Ia	446	2.4–5.0	0.07	0.30 ± 0.10	56	1.06 ± 0.33	1.1 ± 0.4	(8)
G189.1+3.0	IC 443, Jellyfish Nebula	CC	3000–30000	0.7–2.0	0.33 ± 0.01	0.012	165	57.27 ± 1.15	⋯	(9)
G260.4−3.4	Puppis A	CC	3700–4500	1.3–2.2	0.33 ± 0.02	0.13	130	8.04 ± 0.56	⋯	(10)
G266.2−1.2	Vela Jr, RX J0852.0–4622	CC	2400–5100	0.5–1.0	1.19 ± 0.04	0.35 ± 0.13	50	12.11 ± 0.89	200 ± 6.58	(11)
G272.2−3.2		Ia	3600–11000	2.0–10.0	0.12	0.036	0.4	1.2	5.6	(12)
G291.0−0.1		CC	1300–10000	3.5–6.0	0.23	⋯	16	13.04 ± 0.78	4.9	(13)
G292.0+1.8		CC	2930–3050	6.0	0.2	0.043	15	6.17 ± 0.43	3.2	(14)
G296.1−0.5		CC	2800–28000	2.0–4.0	0.25	0.040 ± 0.003	8	2.0	3.6	(15)
G306.3−0.9		Ia	1300–4600	8.0	0.02	0.018 ± 0.001	0.16	1.1	1.1	(16)
G308.4−1.4		CC	5000–7500	9.1–10.7	0.07	0.016 ± 0.004	0.4	0.58	3.5	(17)
G309.2−0.6		CC	700–4000	2.0–6.0	0.11	⋯	7	0.96	3.8	(18)
G315.4−2.3	RCW 86	Ia	2000–10000	2.3–3.2	0.35	0.13 ± 0.06	49	34	18.2 ± 9.4	(19)
G327.6+14.6	SN 1006	Ia	1012	1.6–2.2	0.25	0.29	19	0.72	3.7 ± 0.8	(20)
G330.2+1.0		CC	1000–3000	⩾5.0	0.08	0.20	5	0.64	7.3	(21)
G347.3−0.5	RX J1713.7–3946	CC	1625	1.0	0.53 ± 0.03	0.82 ± 0.06	30	4.94 ± 0.81	146 ± 6	(22)
G350.1−0.3		CC	600–1200	4.5–9.0	0.03	0.11 ± 0.03	6	3.3	1.6	(23)

Notes. The SNR observation data, radio flux from Green (2017), GeV flux from Acero et al. (2016), TeV flux from H.E.S.S. Collaboration et al. (2018a), and the other data from *SNRcat* (available at "http://www.physics.umanitoba.ca/snr/SNRcat/"), and references for each: (1) Carlton et al. (2011), H.E.S.S. Collaboration et al. (2014); (2) Aharonian et al. (2008), Vink (2008); (3) Sasaki et al. (2018); (4) Uchida et al. (2012), Ackermann et al. (2013); (5) Keohane et al. (2007), Zhu et al. (2014); (6) Hui & Becker (2009); (7) DeLaney & Rudnick (2003); (8) Katsuda et al. (2010), Giordano et al. (2012); (9) Ackermann et al. (2013), Ambrocio-Cruz et al. (2017); (10) Reynoso et al. (2017); (11) Allen et al. (2015), H.E.S.S. Collaboration et al. (2018b); (12) Sánchez-Ayaso et al. (2013); (13) Roger et al. (1986); (14) Gaensler & Wallace (2003), Gonzalez & Safi-Harb (2003); (15) Gök & Sezer (2012); (16) Reynolds et al. (2013), Sezer et al. (2017); (17) Prinz & Becker (2012); (18) Rakowski et al. (2001); (19) Helder et al. (2013), H.E.S.S. Collaboration et al. (2018c); (20) Nikolić et al. (2013), Condon et al. (2017); (21) H.E.S.S. Collaboration et al. (2014), Williams et al. (2018); (22) Tsuji & Uchiyama (2016), H.E.S.S. Collaboration et al. (2018a); (23) Lovchinsky et al. (2011).

[a] Type of SN explosion; "Ia" implies thermonuclear explosion, and "CC" implies core-collapse SN. About the SNRs whose explosion type is not known much, it is assumed to be "CC" in this table.

[b] The integrated flux by *Fermi*-LAT in the 1–100 GeV range, but those without error are the 99% confidence upper limit with photon index $\Gamma = 2.5$ because the SNR is not observed by *Fermi*-LAT; see Acero et al. (2016) for details.

[c] The integral flux by H.E.S.S. in the 1–10 TeV range; that with error is the detected value, and that without error is the upper limit of 99% confidence level with $\Gamma = 2.3$.

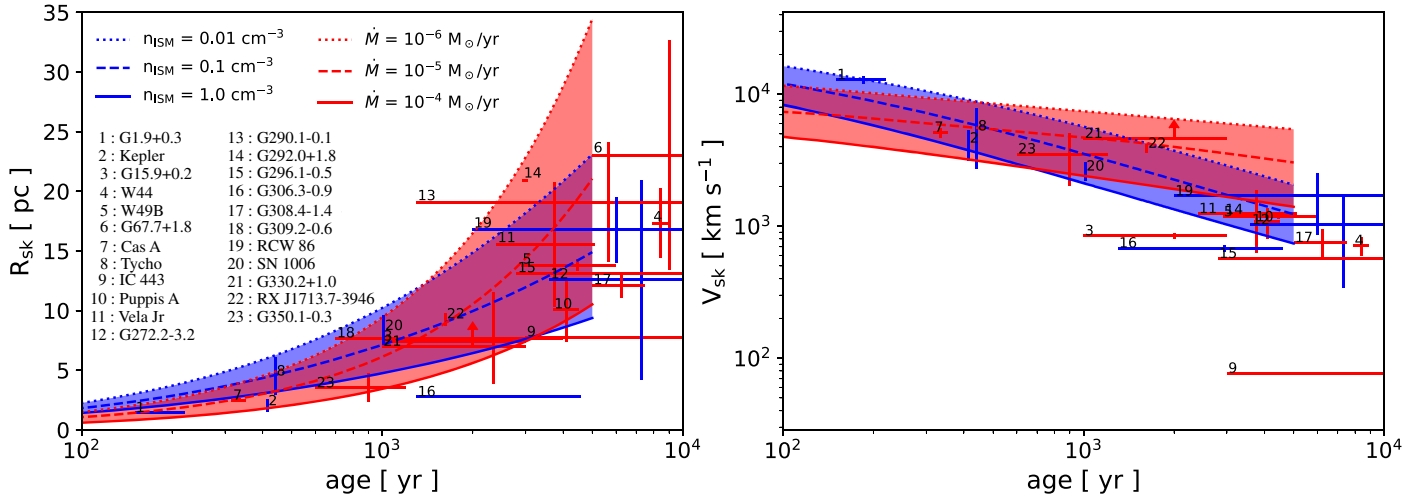

Figure 11. Left panel: FS location as a function of age. Blue (red) dotted, dashed, and solid lines show the results of models A1 (B1), A2 (B2), and A3 (B3), respectively. Right panel: FS velocity as a function of time. The observation data are shown by the blue (Ia) and red (CC) data points in both panels and are summarized in Table 3.

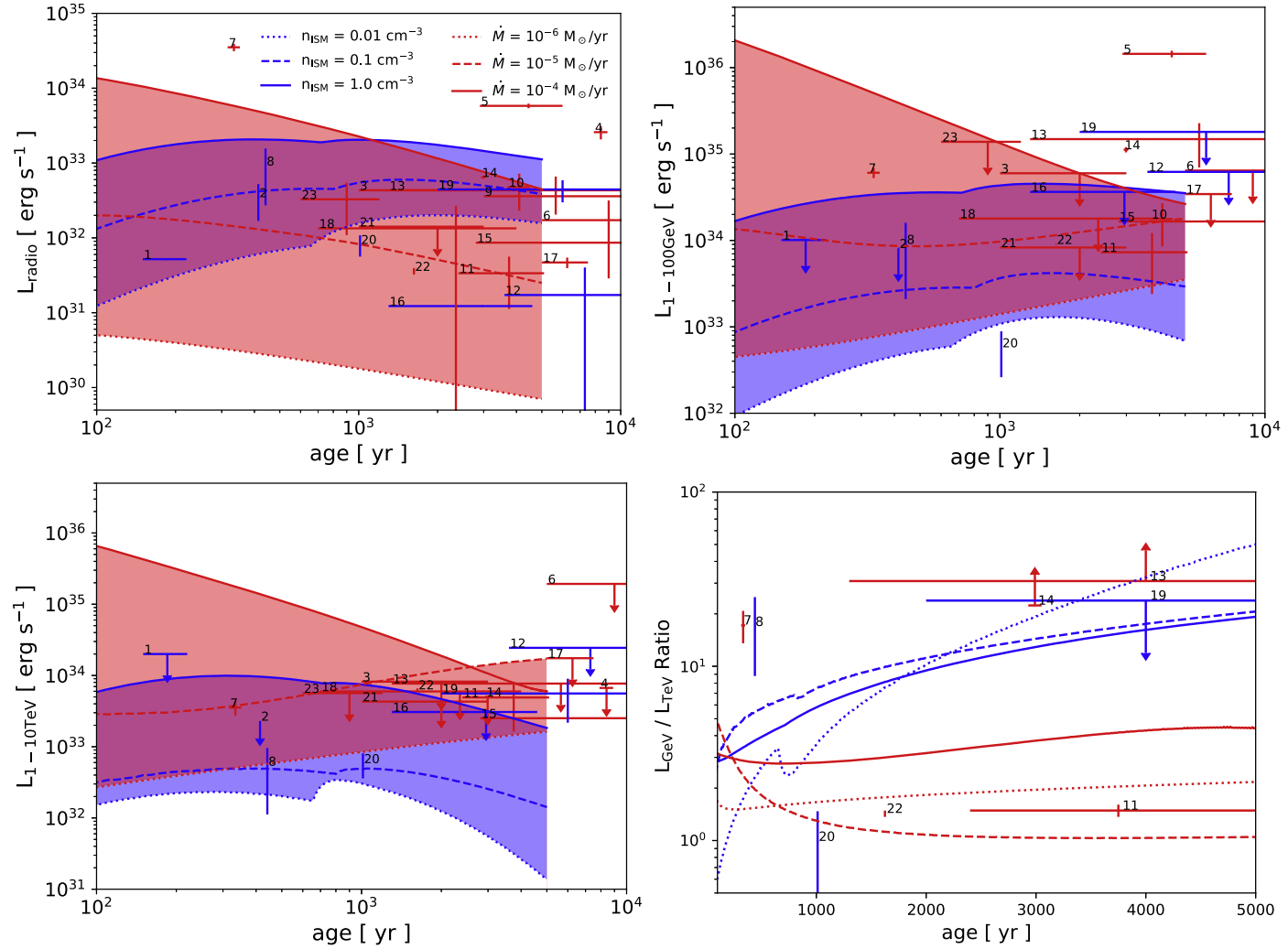

Figure 12. Top left panel: radio luminosity at 1 GHz as a function of time. Top right panel: integrated γ-ray luminosity from 1 GeV to 100 GeV as a function of time. Bottom left panel: integrated γ-ray luminosity from 1 TeV to 10 TeV as a function of time. Bottom right panel: ratio of GeV to TeV luminosity as a function of time. The format of lines and data in all panels is the same as in Figure 11.

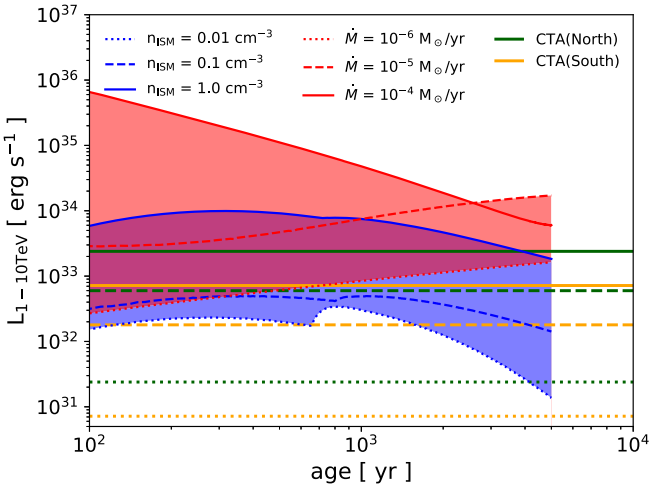

Figure 13. TeV luminosity as a function of time from our models compared with CTA sensitivities assuming different SNR distances. The green (yellow) lines show the sensitivities of CTA at the north (south) site for a source distance of 1.0 kpc (dotted), 5.0 kpc (dashed), and 10.0 kpc (solid).

Here we compare the calculated TeV luminosity from our Type Ia and CC SNR models with the CTA sensitivities to predict the horizons for SNRs residing in different types of ambient environments. Figure 13 shows the range of model TeV luminosity and CTA sensitivities for different source distances. These sensitivities are calculated using the differential sensitivity curve assuming an observation time of 50 hr (see, for details, http://www.cta-observatory.org/science/cta-performance/ (version prod3b-v1)). We do not consider the possibility of source confusion, (fore-)background contamination, and other complications for simplicity.

For SNRs with $d_{\rm SNR} = 1.0$ kpc, we see that, within the parameter range of our models, they are easily detectable regardless of age or ambient environment. For $d_{\rm SNR} = 5.0$ kpc, the detectability starts to depend on the SN type, age, and environment. For both the southern and northern sky, the CC SNRs should be observable irrespective of age and environment. The Type Ia SNRs are also detectable, except for those in the southern sky with $t_{\rm age} \geqslant 2000$ yr interacting with a very tenuous $n_{\rm ISM} \sim 0.01$ cm^{-3} environment, or those in the northern sky with a density $n_{\rm ISM} \leqslant 0.1$ cm^{-3}. For $d_{\rm SNR} = 10.0$ kpc, the sensitivity for the southern sky is roughly the same as that of the northern sky for $d_{\rm SNR} = 5.0$ kpc. SNRs in the northern sky can be detected if the environment is dense, with $n_{\rm ISM} \sim 1.0$ cm^{-3} for a Type Ia in a uniform ISM or $\dot{M} \geqslant 10^{-5}\ M_\odot$ yr^{-1} for a CC in a wind. Hence, letting $n_{\rm ISM} = 0.1$ cm^{-3} and $\dot{M} = 10^{-5}\ M_\odot$ yr^{-1} be the typical values for an ISM-like and a power-law CSM-like environment, respectively, we can conclude that the CTA has a sufficient sensitivity to observe most Type Ia SNRs with $d_{\rm SNR} \leqslant 5.0$ kpc and CC SNRs with $d_{\rm SNR} \leqslant 10.0$ kpc and younger than 5000 yr, provided that they have a particle acceleration efficiency similar to Tycho and RX J1713. These results are encouraging in that the number of the SNRs whose VHE emission will be detected at a distance $d_{\rm SNR} \leqslant 5.0$ kpc will dramatically increase in the CTA era.

4. Conclusion

In this study, we model the time evolution of SNRs using a hydrodynamical simulation coupling with efficient particle acceleration based on previous works (e.g., Blasi 2004; Caprioli et al. 2010a, 2010b; Lee et al. 2012) and investigate how their broadband nonthermal SEDs evolve in various kinds of ambient environments. We prepare three models for the ambient medium, including a uniform ISM-like case for Type Ia SNRs, a power-law CSM from a steady isotropic stellar wind for CC SNRs, and a case with a pre-SN enhanced mass loss from a massive star that creates a dense confined CSM shell surrounding the ejecta.

In the Type Ia models with a uniform ISM, while the π^0-decay flux increases with time, IC flux does not vary much with its spectral peak shifting to lower energy as the SNR ages. In the CC models with a simple power-law CSM, while π^0-decay flux decreases with time, the IC contribution increases with time on the contrary. We found that the key aspects that dictate these evolutionary trends are the density distribution of the interaction targets for each emission component and the rate of energy loss of the electrons due to synchrotron radiation. In our models, since the interaction target is the ambient gas for π^0-decay and the uniform CMB radiation field for IC, the spatial distribution of the ambient gas density is a key to understanding the evolution of the γ-ray spectrum, including a possible transition between a leptonic and a hadronic origin at a certain evolutionary stage. Moreover, the accelerated electrons lose their energy via synchrotron radiation owing to a highly amplified magnetic field in the uniform ISM cases. Our results are consistent with the previously proposed picture that the ISM/CSM gas density decides the dominant component of γ-ray emission from an SNR (e.g., Yuan et al. 2012). In addition, we propose that not only the number density of the ambient environment but also the distribution of magnetic field are important in understanding the time evolution of VHE emission. In the case of an enhanced mass loss from a massive star progenitor, the production of secondary particles is found to be very efficient in the dense confined CSM shell and contributes importantly to the overall SED. For example, they can dominate the synchrotron radiation after the SNR breaks out from the shell into a tenuous wind.

A comparison between our models and observations shows a broad agreement. A dramatic enlargement of the sample size of γ-ray-emitting SNRs is anticipated in the CTA era to further constrain the parameter space in our systematic survey of SNR broadband models. CTA will have a sufficient sensitivity to detect VHE emission from most Type Ia and CC SNRs in various environments with a distance within ~5.0 kpc. Future observations by CTA will reveal the detailed morphological and spectral properties of γ-ray emissions from SNRs and make important progress on our understanding of the particle acceleration mechanism at astrophysical collisionless shocks.

We note that the current study has only examined several simple models for the ambient environment, which in reality can be much more complicated, such as the presence of a cavity, dense shells, clumpy winds, and MCs. Our code is designed to be modular, which makes it easy for us to expand into a broader parameter space, including more complicated models for the environment. In future work, we will also explore other important physics such as the acceleration of heavier ions, thermal X-ray line emission, and radiative shocks.

The authors acknowledge important discussions with K. Maeda concerning this work. S.H.L. acknowledges support from the Kyoto University Foundation.

References

Abdo, A. A., Ackermann, M., Ajello, M., et al. 2010, ApJL, 710, L92
Abdo, A. A., Ackermann, M., Ajello, M., et al. 2011, ApJ, 734, 28
Acciari, V. A., Aliu, E., Arlen, T., et al. 2009, ApJL, 698, L133
Acciari, V. A., Aliu, E., Arlen, T., et al. 2010, ApJ, 714, 163
Acciari, V. A., Aliu, E., Arlen, T., et al. 2011, ApJL, 730, L20
Acero, F., Ackermann, M., Ajello, M., et al. 2016, ApJS, 224, 8
Acero, F., Aharonian, F., Akhperjanian, A. G., et al. 2010, A&A, 516, A62
Acero, F., Ballet, J., Decourchelle, A., et al. 2009, A&A, 505, 157
Ackermann, M., Ajello, M., Allafort, A., et al. 2013, Sci, 339, 807
Aharonian, F., Akhperjanian, A. G., Barres de Almeida, U., et al. 2008, A&A, 488, 219
Aharonian, F., Akhperjanian, A. G., Bazer-Bachi, A. R., et al. 2007, A&A, 464, 235
Aharonian, F., Akhperjanian, A. G., Bazer-Bachi, A. R., et al. 2011, A&A, 531, C1
Aharonian, F. A., Kelner, S. R., & Prosekin, A. Y. 2010, PhRvD, 82, 043002
Ahnen, M. L., Ansoldi, S., Antonelli, L. A., et al. 2017, MNRAS, 472, 2956
Albert, J., Aliu, E., Anderhub, H., et al. 2007, ApJL, 664, L87
Allen, G. E., Chow, K., DeLaney, T., et al. 2015, ApJ, 798, 82
Allen, G. E., Petre, R., & Gotthelf, E. V. 2001, ApJ, 558, 739
Ambrocio-Cruz, P., Rosado, M., de la Fuente, E., Silva, R., & Blanco-Piñon, A. 2017, MNRAS, 472, 51
Archambault, S., Archer, A., Benbow, W., et al. 2017, ApJ, 836, 23
Artyukh, V. S., Vitkevich, V. V., & Dagkesamanskii, R. D. 1967, AZh, 44, 984
Baade, W., & Zwicky, F. 1934, PNAS, 20, 259
Bamba, A., Fukazawa, Y., Hiraga, J. S., et al. 2008, PASJ, 60, S153
Baring, M. G., Ellison, D. C., Reynolds, S. P., Grenier, I. A., & Goret, P. 1999, ApJ, 513, 311
Bell, A. R. 1978, MNRAS, 182, 147
Blasi, P. 2004, APh, 21, 45
Blasi, P., Gabici, S., & Vannoni, G. 2005, MNRAS, 361, 907
Blondin, J. M., & Ellison, D. C. 2001, ApJ, 560, 244
Caprioli, D., Amato, E., & Blasi, P. 2010a, APh, 33, 307
Caprioli, D., Blasi, P., & Amato, E. 2009a, MNRAS, 396, 2065
Caprioli, D., Blasi, P., Amato, E., & Vietri, M. 2009b, MNRAS, 395, 895
Caprioli, D., Kang, H., Vladimirov, A. E., & Jones, T. W. 2010b, MNRAS, 407, 1773
Carlton, A. K., Borkowski, K. J., Reynolds, S. P., et al. 2011, ApJL, 737, L22
Castelletti, G., Dubner, G., Brogan, C., & Kassim, N. E. 2007, A&A, 471, 537
Castelletti, G., Dubner, G., Clarke, T., & Kassim, N. E. 2011, A&A, 534, A21
Chevalier, R. A. 1982a, ApJ, 258, 790
Chevalier, R. A. 1982b, ApJL, 259, L85
Condon, B., Lemoine-Goumard, M., Acero, F., & Katagiri, H. 2017, ApJ, 851, 100
DeLaney, T., & Rudnick, L. 2003, ApJ, 589, 818
Drury, L. 1983, SSRv, 36, 57
Duncan, A. R., & Green, D. A. 2000, A&A, 364, 732
Dwarkadas, V. V., & Chevalier, R. A. 1998, ApJ, 497, 807
Ellison, D. C., Slane, P., Patnaude, D. J., & Bykov, A. M. 2012, ApJ, 744, 39
Fang, J., & Zhang, L. 2008, MNRAS, 384, 1119
Fermi, E. 1949, PhRv, 75, 1169
Ferrand, G., & Safi-Harb, S. 2012, AdSpR, 49, 1313
Fukui, Y., Sano, H., Sato, J., et al. 2012, ApJ, 746, 82
Gaensler, B. M., & Wallace, B. J. 2003, ApJ, 594, 326
Gaggero, D., Zandanel, F., Cristofari, P., & Gabici, S. 2018, MNRAS, 475, 5237
Giordano, F., Naumann-Godo, M., Ballet, J., et al. 2012, ApJL, 744, L2
Giuliani, A., Cardillo, M., Tavani, M., et al. 2011, ApJL, 742, L30
Gök, F., & Sezer, A. 2012, MNRAS, 419, 1603
Gonzalez, M., & Safi-Harb, S. 2003, ApJL, 583, L91
Green, D. A. 2017, yCat, 7278, 0
Helder, E. A., Vink, J., Bamba, A., et al. 2013, MNRAS, 435, 910
H.E.S.S. Collaboration, Abdalla, H., Abramowski, A., et al. 2018a, A&A, 612, A6
H.E.S.S. Collaboration, Abdalla, H., Abramowski, A., et al. 2018b, A&A, 612, A7
H.E.S.S. Collaboration, Abramowski, A., Aharonian, F., et al. 2014, MNRAS, 441, 790
H.E.S.S. Collaboration, Abramowski, A., Aharonian, F., et al. 2015, A&A, 575, A81
H.E.S.S. Collaboration, Abramowski, A., Aharonian, F., et al. 2018c, A&A, 612, A4
Hewitt, J. W., Grondin, M.-H., Lemoine-Goumard, M., et al. 2012, ApJ, 759, 89
Hui, C. Y., & Becker, W. 2009, A&A, 494, 1005
Kamae, T., Karlsson, N., Mizuno, T., Abe, T., & Koi, T. 2006, ApJ, 647, 692
Katsuda, S., Petre, R., Hughes, J. P., et al. 2010, ApJ, 709, 1387
Keohane, J. W., Reach, W. T., Rho, J., & Jarrett, T. H. 2007, ApJ, 654, 938
Kothes, R., Fedotov, K., Foster, T. J., & Uyanıker, B. 2006, A&A, 457, 1081
Lazendic, J. S., Slane, P. O., Gaensler, B. M., et al. 2004, ApJ, 602, 271
Lee, S.-H., Ellison, D. C., & Nagataki, S. 2012, ApJ, 750, 156
Lee, S.-H., Patnaude, D. J., Raymond, J. C., et al. 2015, ApJ, 806, 71
Lovchinsky, I., Slane, P., Gaensler, B. M., et al. 2011, ApJ, 731, 70
Maeda, Y., Uchiyama, Y., Bamba, A., et al. 2009, PASJ, 61, 1217
Matsumoto, Y., Amano, T., Kato, T. N., & Hoshino, M. 2017, PhRvL, 119, 105101
Nicholl, M., Smartt, S. J., Jerkstrand, A., et al. 2015, MNRAS, 452, 3869
Nikolić, S., van de Ven, G., Heng, K., et al. 2013, Sci, 340, 45
Planck Collaboration, Arnaud, M., Ashdown, M., et al. 2016, A&A, 586, A134
Prinz, T., & Becker, W. 2012, A&A, 544, A7
Rakowski, C. E., Hughes, J. P., & Slane, P. 2001, ApJ, 548, 258
Reynolds, M. T., Loi, S. T., Murphy, T., et al. 2013, ApJ, 766, 112
Reynoso, E. M., Cichowolski, S., & Walsh, A. J. 2017, MNRAS, 464, 3029
Roger, R. S., Milne, D. K., Caswell, J. L., & Little, A. G. 1986, MNRAS, 219, 815
Rybicki, G. B., & Lightman, A. P. 1986, Radiative Processes in Astrophysics (Oxford: Wiley), 400
Sánchez-Ayaso, E., Combi, J. A., Bocchino, F., et al. 2013, A&A, 552, A52
Sasaki, M., Mäkelä, M. M., Klochkov, D., Santangelo, A., & Suleimanov, V. 2018, MNRAS, 479, 3033
Sedov, L. I. 1959, Similarity and Dimensional Methods in Mechanics (New York: Academic Press)
Sezer, A., Ergin, T., & Yamazaki, R. 2017, MNRAS, 466, 3434
Sinitsina, V. G., & Sinitsina, V. Y. 2015, BuLPI, 42, 169
Slane, P., Lee, S.-H., Ellison, D. C., et al. 2014, ApJ, 783, 33
Spitzer, L. 1965, Physics of Fully Ionized Gases (New York: Interscience)
Sturner, S. J., Skibo, J. G., Dermer, C. D., & Mattox, J. R. 1997, ApJ, 490, 619
Tanaka, T., Allafort, A., Ballet, J., et al. 2011, ApJL, 740, L51
Tanaka, T., Uchiyama, Y., Aharonian, F. A., et al. 2008, ApJ, 685, 988
Tang, Z., Reynolds, S. P., & Ressler, S. M. 2016, ApJS, 227, 28
Tavani, M., Giuliani, A., Chen, A. W., et al. 2010, ApJL, 710, L151
Troja, E., Segreto, A., La Parola, V., et al. 2014, ApJL, 797, L6
Truelove, J. K., & McKee, C. F. 1999, ApJS, 120, 299
Tsuji, N., & Uchiyama, Y. 2016, PASJ, 68, 108
Uchida, H., Koyama, K., Yamaguchi, H., et al. 2012, PASJ, 64, 141
Vink, J. 2008, ApJ, 689, 231
Wang, C.-Y., & Chevalier, R. A. 2001, ApJ, 549, 1119
Wang, W., & Li, Z. 2016, ApJ, 825, 102
Warren, D. C., & Blondin, J. M. 2013, MNRAS, 429, 3099
Warren, J. S., Hughes, J. P., Badenes, C., et al. 2005, ApJ, 634, 376
Williams, B. J., Borkowski, K. J., Ghavamian, P., et al. 2013, ApJ, 770, 129
Williams, B. J., Hewitt, J. W., Petre, R., & Temim, T. 2018, ApJ, 855, 118
Xin, Y.-L., Guo, X.-L., Liao, N.-H., et al. 2017, ApJ, 843, 90
Yuan, Q., Liu, S., & Bi, X. 2012, ApJ, 761, 133
Zhu, H., Tian, W. W., & Zuo, P. 2014, ApJ, 793, 95